

Spatial and temporal influence of rainfall on crustal pore pressure based on seismic velocity monitoring

Rezkie Dewi Andajani

Kyushu University

Takeshi Tsuji (✉ tsuji@mine.kyushu-u.ac.jp)

Kyushu University <https://orcid.org/0000-0003-0951-4596>

Roel Snieder

Colorado School of Mines

Tatsunori Ikeda

Kyushu University

Full paper

Keywords: seismic velocity variation, rain precipitation, groundwater level, pore pressure, near-surface lithology, monitoring

Posted Date: November 6th, 2020

DOI: <https://doi.org/10.21203/rs.3.rs-33211/v3>

License: © ⓘ This work is licensed under a Creative Commons Attribution 4.0 International License.

[Read Full License](#)

Version of Record: A version of this preprint was published on November 24th, 2020. See the published version at <https://doi.org/10.1186/s40623-020-01311-1>.

1 **Spatial and temporal influence of rainfall on crustal pore**
2 **pressure based on seismic velocity monitoring**

3

4 Rezkia Dewi Andajani¹

5 ¹Department of Earth Resources Engineering, Kyushu University, 744 Motooka, Nishi-
6 ku, Fukuoka 819-0395, Japan (Email: rezkiadewiandajani90@mine.kyushu-u.ac.jp).

7

8 Takeshi Tsuji^{1,2,3*}

9 ¹Department of Earth Resources Engineering, Kyushu University, 744 Motooka, Nishi-
10 ku, Fukuoka 819-0395, Japan. ² International Institute for Carbon-Neutral Energy
11 Research (WPI-I2CNER), Kyushu University, 744 Motooka, Nishi-ku, Fukuoka 819-0395,
12 Japan. ³Disaster Prevention Research Institute, Kyoto University Gokasho, Uji, Kyoto,
13 611-0011, Japan (Email: tsuji@mine.kyushu-u.ac.jp).

14

15 Roel Snieder⁴

16 ⁴Colorado School of Mines. Hill Hall 206A, Golden CO, 80401-1887, USA. (Email:
17 rsnieder@mines.edu)

18

19 Tatsunori Ikeda^{1,2},

20 ¹Department of Earth Resources Engineering, Kyushu University, 744 Motooka, Nishi-
21 ku, Fukuoka 819-0395, Japan. ² International Institute for Carbon-Neutral Energy
22 Research (WPI-I2CNER), Kyushu University, 744 Motooka, Nishi-ku, Fukuoka 819-0395,
23 Japan (Email: ikeda@mine.kyushu-u.ac.jp).

24

25 *Corresponding author: Takeshi Tsuji (tsuji@mine.kyushu-u.ac.jp)

26

27 **Abstract**

28 Crustal pore pressure, which controls the activities of earthquakes and volcanoes, varies
29 in response to rainfall. The status of pore pressure can be inferred from observed
30 changes in seismic velocity. In this study, we investigate the response of crustal pore
31 pressure to rainfall in southwestern Japan based on time series of seismic velocity
32 derived from ambient noise seismic interferometry. To consider the heterogeneity of
33 the area, rainfall and seismic velocity obtained at each location were directly compared.
34 We used a band-pass filter to distinguish the rainfall variability from sea level and
35 atmospheric pressure, and then calculated the cross-correlation between rainfall and
36 variations in S-wave velocity (V_s). A mostly negative correlation between rainfall and V_s
37 changes indicates groundwater recharge by rainfall, which increases pore pressure. The
38 correlations differ between locations, where most of the observation stations with clear
39 negative cross-correlations were located in areas of granite. On the other hand, we
40 could not observe clear correlations in steep mountain areas, possibly because water
41 flows through river without percolation. This finding suggests that geographical features
42 contribute to the imprint of rainfall on deep formation pore pressure. We further
43 modelled pore pressure change due to rainfall based on diffusion mechanism. A strong
44 negative correlation between pore pressure estimated from rainfall and V_s indicates
45 that the V_s variations are triggered by pore pressure diffusion in the deep formation.
46 Our modelling results show a spatial variation of diffusion parameter which controls the
47 pore pressure in deep formation. By linking the variations in seismic velocity and crustal

48 pore pressure spatially, this study shows that seismic monitoring may be useful in
49 evaluating earthquake triggering processes or volcanic activity.

50

51 **Keywords:** seismic velocity variation, rain precipitation, groundwater level, pore
52 pressure, near-surface lithology, monitoring

53

54 **1. Introduction**

55 Pore pressure plays a key role in the occurrence of earthquakes and the volcanic
56 activities (Albino et al. 2018; Ellsworth 2013; Tsuji et al., 2014). Under conditions of
57 critical stress and high pore pressure, small increases in pore pressure can trigger
58 seismicity. Therefore, monitoring the status of pore pressure is a vital part of evaluating
59 dynamic crustal activities. Because pore pressure affects seismic velocity, the state of
60 pore pressure can be assessed by seismic velocity monitoring (Chaves and Schwartz
61 2016; Hutapea et al., 2020; Ikeda and Tsuji 2018; Nimiya et al. 2017; Rivet et al. 2015;
62 Tsuji et al. 2008; Wang et al. 2017).

63 In field observations, changes in seismic velocity can be induced by various
64 environmental perturbations (Wang et al. 2017) because seismic velocity is sensitive to
65 variations in stress and water saturation (Grêt et al. 2006). Such perturbations include
66 ocean tides and solid earth tides (Sens-Schönfelder and Eulenfeld 2019), and seismic
67 velocity in coastal locations is sensitive to tidal ocean loading (Yamamura et al. 2003).
68 The influence of the ocean is considered in studies of ambient seismic noise (Hillers et

69 al. 2012). Atmospheric pressure influences seismic velocity over large regions (Niu et al.
70 2008; Silver et al. 2007), and atmospheric temperature likewise generates seasonal
71 variations in seismic velocity through changes in crustal strain (Ben-Zion and Leary 1986;
72 Berger 1975; Prawirodirdjo et al. 2006), especially in arid regions (Hillers et al. 2015;
73 Richter et al. 2014).

74 Rainfall and snow are well-known hydrological perturbations by which pore pressure
75 induces seismic velocity changes. For example, the interaction of hydrothermal systems
76 and surface loading from precipitation can lead to seismic velocity reductions (Taira and
77 Brenguier 2016). Snow decreases seismic velocity through increased pore pressure
78 resulting from ice infiltration (Mordret et al. 2016) whereas frost increases seismic
79 velocity at shallow depths by increasing the shear modulus of near-surface materials
80 (Gassenmeier et al. 2015; Ikeda et al. 2018; Tsuji et al., 2012). Rainfall decreases seismic
81 velocity through changes in effective stress (Nakata and Snieder 2012; Miao et al. 2018)
82 and groundwater level (Gassenmeier et al. 2015; Meier et al. 2010; Sens-Schönfelder
83 and Wegler 2006; Tsai 2011). Rainfall triggers seismicity through pore pressure changes
84 caused by crustal loading and unloading (Bettinelli et al. 2008) and pore pressure
85 diffusion (Hainzl et al. 2006; Kraft et al. 2006). Because percolation of water through
86 porous rock may be a contributor to pore pressure changes, we investigated the spatial
87 and temporal relationships between seismic velocity changes and rainfall in a well-
88 instrumented region of Japan.

89 Crustal deformation in Japan can be evaluated with abundant data from seismic and
90 geodetic observation stations (Aoi et al., 2020). The crust is affected by perturbations

91 from volcanic and seismic activities (Ueda et al. 2013) and surface loads (Heki 2004),
92 including non-tidal ocean loading (Sato et al. 2001). Recent studies have shown that
93 observed seismic velocity changes reflect volcanic activity (Takano et al. 2017; Yukutake
94 et al. 2016) and earthquake activity (Nimiya et al. 2017). Furthermore, seasonal spatial
95 patterns of seismic velocity change throughout Japan can be explained by seasonal
96 variations in rainfall, snow, and sea level (Wang et al. 2017).

97 This study uses records of seismic velocity changes estimated from ambient noise
98 monitoring in the Chugoku and Shikoku regions of southwest Japan (Fig. 1). This area
99 receives high rainfall from the summer monsoon (Aizen et al. 2001) and is relatively
100 unaffected by volcanic activity and snowfall. To evaluate the influence of rainfall on
101 seismic velocity changes, we performed two step analyses. In the first step, we sought
102 to identify locations where seismic velocity could be affected by rainfall by directly
103 comparing the seismic velocity to the rainfall via cross-correlations (e.g., Bièvre et al.
104 2018). The time delay resulting from the cross-correlations helps to constrain near-
105 surface conditions that could be related to lithology-related permeability. In the second
106 step, we modelled pore pressure change due to pore pressure diffusion to estimate a
107 hydrological parameter (i.e., diffusion rate) for the locations where precipitation
108 influence was clearly estimated in the first step. By comparing the seismic velocity
109 change and modelled pore pressure change, we sought to estimate spatial variation of
110 the diffusion parameter in deeper lithology which contributes to predicting
111 precipitation-related pore pressure changes from seismic velocity in Chugoku and
112 Shikoku region.

113 Well-quantified monitoring results could be useful information for the evaluation of
114 earthquake triggering mechanisms. In CO₂ geological storage projects and geothermal
115 developments, furthermore, earthquakes induced by fluid injection are a notable public
116 concern. Accurate knowledge of natural pore pressure variations can help in
117 distinguishing whether an earthquake is a natural event triggered by environmental
118 variations or an induced event triggered by fluid invasion.

119

120 **2. Data preparation**

121 The Chugoku and Shikoku regions are located in southwest Japan (Fig. 1). The
122 Chugoku region is characterized by mountainous topography with gently sloping, while
123 the slopes of the mountains in Shikoku island are mostly steep (Fig. 1b). Fig. 1c shows
124 the rock types of our study area from the geological map (Geological Survey of Japan
125 AIST, 2015). The Chugoku region is abundant with Cretaceous volcanic and granitic
126 rocks, along with granitic rocks from the Paleocene to the early Eocene, and Late
127 Pleistocene to Holocene sediments at the northern Chugoku. As for the Shikoku region,
128 Late Cretaceous granite can be found in the northern Shikoku, while Sanbagawa
129 metamorphic rocks are widely distributed across the centre of the Shikoku. Sandstone
130 of Cretaceous – Oligocene accretionary complexes is mainly located in the southern
131 Shikoku island (steep mountain).

132 We collected data on seismic velocity changes, precipitation, atmospheric
133 pressure, and sea-level change for the period 2015–2017 in the Chugoku and Shikoku
134 regions. The meteorological data was obtained from the Japan Meteorological Agency

135 (JMA) and we used seismic data from 98 seismometers operated by the National
136 Research Institute for Earth Science and Disaster Resilience (NIED). For each Hi-net
137 station, a three-component sensor of the particle velocity with a natural frequency of
138 1Hz is installed in the bottom of the borehole (Obara et al., 2005).

139 We estimated seismic velocity changes on the basis of ambient-noise coda wave
140 interferometry using the vertical component of ambient noise (Hutapea et al. 2020;
141 Nimiya et al. 2017). To obtain virtual seismograms propagating between pairs of
142 stations, two traces of $f_A(t)$ and $f_B(t)$ recorded at seismometers A and B were
143 transformed into frequency domain by the Fourier transform:

144

$$145 \quad F_A(\omega) = \frac{1}{2\pi} \int_{-\infty}^{\infty} f_A(t) e^{-i\omega t} dt$$
$$146 \quad F_B(\omega) = \frac{1}{2\pi} \int_{-\infty}^{\infty} f_B(t) e^{-i\omega t} dt, \quad (1)$$

147

148 where F_A and F_B are the seismic waveforms in the frequency domain (ω) recorded at
149 seismometers A and B.

150 The power-normalized cross-correlation (cross-coherence) was applied in the
151 frequency domain between seismometers at sites A and B (e.g., Nakata et al. 2011,
152 2015) by

153

$$154 \quad CC_{AB}(\omega) = \frac{F_A(\omega) F_B^*(\omega)}{|F_A(\omega)| |F_B(\omega)|}, \quad (2)$$

155

156 where the asterisk (*) denotes a complex conjugate.

157 Changes in seismic velocity between pairs of seismometers were estimated by the
 158 stretching interpolation method (Hadziioannou et al. 2009; Hutapea et al. 2020; Minato
 159 et al. 2012; Nimiya et al. 2017). This method elongates the time axis and looks for the
 160 trace most similar to the reference trace by means of the correlation coefficient $CC(\varepsilon)$
 161 between the reference trace and the current trace:

162

$$163 \quad CC(\varepsilon) = \frac{\int f_{\varepsilon}^{cur}(t) f^{ref}(t) dt}{(\int (f_{\varepsilon}^{cur}(t))^2 dt \int (f^{ref}(t))^2 dt)^{1/2}}, \quad (3)$$

164

$$165 \quad f_{\varepsilon}^{cur}(t) = f^{cur}(t(1 + \varepsilon)), \quad (4)$$

166

167 where f^{ref} is the reference trace, f^{cur} is the current trace, and t is time. The stretching
 168 parameter ε is related to the relative time-shift ($\Delta t/t$) and velocity change ($\Delta v/v$) from

169

$$170 \quad \varepsilon = \Delta t/t = -(\Delta v/v). \quad (5)$$

171

172 The time window of 100 s for coda waves was used to obtain velocity changes by
 173 the stretching interpolation. The seismic velocity change was estimated independently
 174 for each individual year by defining the 1-year stack of the coda of cross-correlation data
 175 as the reference trace f^{ref} and the 10-day stack of the coda of cross-correlation data as
 176 the current trace f^{cur} . To stabilize the monitoring results over the 3-year term, we used
 177 the Sliding Reference Method (SRM) to define the reference trace (see Hutapea et al.

178 2020). In the SRM method, we changed the reference trace for each year. For example,
179 to estimate daily seismic velocity changes in 2015, we defined the coda of cross-
180 correlation stacking over the whole year of 2015 as the reference trace. The daily
181 velocity change was considered to represent the velocity change in the middle of the 10-
182 day window of the current trace. The frequency range of the seismic data was restricted
183 to 0.1 to 0.9 Hz, which reflects the sensitivity of surface waves to S-wave velocity
184 between depths of 1 and 8 km (e.g., Nimiya et al. 2017). To obtain seismic velocity
185 changes for each station (Fig. 1d), we applied spatial averaging within a radius of 40 km.

186 To obtain precipitation data for each seismic station, we averaged the data from
187 all precipitation gauges within a distance of less than 40 km from the seismic stations
188 (Fig. 1e). Atmospheric pressure and sea-level changes were obtained from the tidal
189 gauge closest to the seismic station (Fig. 1f) and the daily sea-level change was estimated
190 by averaging data for the most recent 24-h period.

191

192 **3. Methods**

193 Several studies have linked changes in seismic velocity to groundwater recharge
194 by rain precipitation (e.g., Gassenmeier et al. 2015; Sens-Schönfelder and Wegler 2006).
195 When surface water from precipitation replenishes groundwater, we expect decrease in
196 seismic velocity reflecting pore pressure increase due to (a) immediate loading in
197 undrained condition (impermeable), and (b) pore pressure diffusion (Talwani 1997). To
198 confirm the effect of precipitation on changes in seismic velocity, we applied two-step
199 analyses.

200 In the first step, the time delay between precipitation and seismic velocity
201 change is estimated by cross-correlating the two time series. We identify the locations
202 where velocity changes occurred after precipitations, indicating the influence of pore
203 pressure change due to groundwater recharge. Because the quasi-annual period of
204 seismic velocity change could be influenced by other environmental factors (e.g.,
205 atmospheric pressure and sea level), we apply a bandpass filter in order to clearly
206 distinguish rainfall from sea level and atmospheric pressure. Therefore, in the first step,
207 we focus on shorter period fluctuations associated with rain precipitation.

208 In the second step, we focus on locations where precipitation influence on
209 seismic velocity is clearly identified from the first step. We model pore pressure change
210 based on a diffusion mechanism by groundwater load and compare that with the longer
211 period of seismic velocity change to estimate diffusion rate in deep lithology. Although
212 the observed response is mostly a coupled mechanism (i.e., undrained response and
213 pore pressure diffusion), the effect of pore pressure diffusion may be dominant in the
214 later time, as the pore pressure increase due to diffusion occurs once the immediate
215 loading has dissipated (Talwani 1997). The longer period velocity variation may include
216 the influence of sea level and atmospheric pressure effects, but the seismic velocity
217 variation we used here does not include strong annual features associated with sea level
218 and atmospheric pressure. We summarized the flow of these two step analyses in the
219 flowchart ([Fig. 2](#)).

220

221 **3.1. Step1: Investigation of the rainfall infiltration**

222 To determine an optimal frequency band to clearly distinguish precipitation
223 influences from other environmental factors, we first investigated the power spectra of
224 seismic velocity changes, precipitation, sea-level changes, and atmospheric pressure
225 changes (Fig S1a). Whereas the power spectrum of seismic velocity changes decreased
226 toward a frequency of 0.1 cycle/day, the spectra of precipitation, sea-level, and
227 atmospheric pressure change showed similar peaks at 0.0018–0.0036 cycle/day, a
228 frequency band close to the annual cycle (Fig. S1b). The similarity of these three peaks
229 meant that the long-term estimated seismic velocity changes could be affected not only
230 by precipitation, but also by sea-level and atmospheric pressure changes.

231 We excluded frequencies below 0.0036 cycle/day to remove the annual seasonal
232 influence of sea-level and atmospheric pressure changes, and we excluded frequencies
233 above 0.05 cycle/day to eliminate the neap and spring tides of sea-level change and the
234 decreasing spectrum of seismic velocity change. We then searched for the frequency
235 band where precipitation could best be distinguished from sea-level change and
236 atmospheric pressure change, as indicated by weak correlations between precipitation
237 and the other two variables. We applied a band-pass filter for periods between 20 and
238 137 days (0.05 to 0.0073 cycle/day; Fig. S1c and S1d) and sought minima in the
239 correlation coefficients between precipitation and sea-level change and between
240 precipitation and atmospheric pressure change, based on the data for all stations. The
241 correlation coefficients were based on the Pearson correlation,

242

$$243 \quad \rho(A, B) = \frac{\text{cov}(A, B)}{\sigma_A \sigma_B}, \quad (6)$$

244

245 where $cov(A, B)$ is the covariance of time series A and B, and σA and σB are the
246 standard deviations of time series A and B.

247 Fig. 3 shows an example of the unfiltered and filtered data for one seismic station
248 (N.YSHH; red dot in Fig. 1f). Seismic velocity changes in Fig.3a represent the averaged
249 velocity change within a 40 km radius. The unfiltered data are colored by the stretching
250 correlation coefficient, averaged for station pairs used to estimate the velocity change.
251 In general, the mean correlation coefficient for station pairs used in this study is above
252 0.5, and the value is even higher in the period when precipitation is relatively high (e.g.,
253 August - November). This indicates the daily seismic velocity change in the study area is
254 stable. Figs. 3b-3d show the time series of precipitation, sea level, and atmospheric
255 pressure, respectively. Because the Pearson correlation value between rainfall and sea
256 level is very small (Fig. 3e), we can use band-pass filtering to separate the imprint of
257 precipitation and sea level, as well as precipitation and atmospheric pressure. The
258 correlation coefficients between band-pass filtered precipitation and sea-level and
259 between precipitation and atmospheric pressure change, respectively, are shown in Fig.
260 4 for all stations. The small correlation coefficients indicate that rainfall is distinguishable
261 from sea-level and atmospheric pressure changes.

262 To further analyse the dependence of seismic velocity changes on rainfall, we applied
263 various time shifts to the rainfall record and evaluated the resulting cross-correlations
264 with seismic velocity changes, as depicted in Fig. 5. Under the assumption that seismic
265 velocity changes are triggered by precipitation after a time lag, we restricted ourselves

266 to positive time lags (i.e., velocity variation after precipitation) and determined the time
267 shift that produced the largest Pearson correlation coefficient.

268 Although we focus on the shorter cycle (shorter than annual period) in order to
269 clarify the relationship between precipitation and velocity change, it is difficult to
270 distinguish the effects of (a) undrained due to loading and (b) diffusion. Thus, in the next
271 investigation, we evaluate the pore pressure diffusion via modeling.

272

273 **3.2. Step2: Investigation of pore pressure diffusion**

274 To calculate the pore pressure change, we use the poroelastic model developed by
275 Talwani et al. (2007). The pore pressure due to diffusion can be described as:

$$276 \quad P_k = \sum_{k=1}^n \delta p_k \operatorname{erfc} \left[\frac{r}{(4c\delta t_k)^{1/2}} \right], \quad (7)$$

277 where δp_i is the water level change, r is the depth from the surface, c indicates the
278 hydraulic diffusion, and δt_k indicates the time increment from the starting time k to n
279 , and erfc denotes error complementary function. Although Talwani et al. (2007) also
280 proposed equation for the pore pressure changes due to undrain loading, the effect is
281 smaller than the diffusion in longer period. Here, we consider the contribution of
282 precipitation from 365 days in the past, thus current pore pressure change is calculated
283 by using the summation of pore pressure change from the previous 365 days. We
284 defined water level change from 2015 to 2017 as the deviation from the average
285 precipitation over 2014.

286 To evaluate the longer period variation, we applied a moving average with 130
287 days windows for seismic velocity change without bandpass filtering in the first step. By

288 comparing seismic velocity changes with the pore pressure changes computed based on
289 equation (7), we estimate the optimum hydraulic diffusion at each station. However, in
290 the calculation of the pore pressure changes, it is difficult to constrain the dependence
291 of the hydraulic diffusion with depth because the relative values of the both parameters
292 in r/\sqrt{c} is sensitive to the calculation of the pore pressure by equation (7). Therefore,
293 we estimate optimum values of c assuming values of r (i.e., depth), by computing
294 correlation coefficients between observed velocity changes and modelled pore pressure
295 changes. Since we expect decrease in seismic velocity due to increase in pore pressure,
296 we determine the optimum value of c with the largest negative correlation. After
297 optimum values of c are estimated at each station and depth, we construct a map of c .

298

299 **4. Results**

300 An example of correlation of rainfall and velocity change at a station near the middle
301 of the study area (red dots in Fig.1f) is shown in Fig. 6. Fig. 6 includes a correlation
302 without band-pass filtering (Fig. 6a), then after band-pass filtering (Fig. 6b), and then
303 after shifting the precipitation record by 8 days to fit the respective peaks (Fig. 6c). This
304 8-day time shift raised the correlation coefficient for the three years' data by more than
305 half, although it is still relatively small at -0.33 . However, when we restricted the
306 comparison to the rainy season (in this case, June to July of 2016 and 2017), the
307 correlation coefficient is much greater (-0.7).

308 For most stations there is a negative correlation between rainfall events and seismic
309 velocity changes (Figs. 7a, 7b); however, a few stations had positive correlations (Fig.
310 7c). The highest absolute value of these correlations, even after applying the optimum
311 time lag, was approximately 0.3 (Fig. 8). This value is not high because several factors
312 may weaken the correlation between seismic velocity changes and rainfall events. For
313 example, random noise in both of the time series and the time windows decreases the
314 coefficient. In the latter case, a short time window for stacking cross-correlations (10
315 days in this study) was necessary to analyse the short-term seismic velocity changes
316 induced by precipitation. A longer time window would improve the stability of the
317 velocity change estimate, but would reduce its temporal resolution (Hutapea et al.
318 2020). Another possibility is that an external factor other than precipitation also
319 influences seismic velocity, such as atmospheric pressure, which can exert effects even
320 at seismogenic depths (Niu et al. 2008).

321 Fig. 8a shows the correlation coefficients between rainfall and seismic velocity for all
322 stations, after applying the optimum time lag for each station. Among these stations, 26
323 stations had absolute correlation coefficients smaller than 0.1, 35 stations had absolute
324 correlation coefficients of 0.1 to 0.2, and 37 stations had absolute correlation
325 coefficients greater than 0.2. We selected the third group with high absolute correlation
326 for further analysis because these stations are clustered and information regarding time
327 lag is reliable only if there is a sufficiently strong correlation. Because most of these
328 stations had a negative correlation between precipitation and seismic velocity, we

329 focused on the stations in this group with negative correlations. These selected stations
330 are shown in [Fig. 8b](#), and their respective time lags are shown in [Fig. 8c](#).

331 To validate the groundwater recharge due to precipitation, we compared the records
332 of rainfall and groundwater level variations. [Figs. 9a and 9b](#) show the unfiltered records
333 for an example station (see [Figs. 1d, 1e, 1f](#)) and the calculated cross-correlation between
334 band-pass filtered precipitation and groundwater level. As shown in [Fig. 9c](#), it takes 5
335 days for rainfall to recharge groundwater, whereas [Fig. 9d](#) shows that rainfall is most
336 strongly correlated with a decrease in seismic velocity 9 days later. The small difference
337 in the time lags between [Fig. 9c](#) (5 days) and [Fig. 9d](#) (9 days) supports our interpretation
338 that the increased groundwater load due to recharge by rainfall causes a subsequent
339 decrease in seismic velocity. We show the influence of the near-surface lithology
340 associated with the rainfall infiltration in [Fig. 10](#).

341 Using the stations where seismic velocity changes are likely influenced by
342 precipitation in [Fig. 8](#), we estimated the optimum value of c by comparing the pore
343 pressure change with seismic velocity change. In [Fig. 11](#), we show an example of
344 comparison between seismic velocity change and pore pressure change with the
345 diffusion rate of $0.14 \text{ m}^2/\text{s}$ for depth of 1.5 km that gives the largest negative correlation
346 at the station of N.YSHH (red dot in [Fig. 1f](#)). [Fig. 12a](#) shows a correlation of the pore
347 pressure and seismic velocity changes for the selected stations in Chugoku and Shikoku
348 region. Several stations in the Chugoku and Shikoku area show relatively weak negative
349 correlation between pore pressure and seismic velocity change (<0.2). This can be due
350 to several possibilities; the diffusion is not dominant at these stations, or other

351 perturbations influence the longer-term variations in seismic velocity. [Fig. 12b](#) shows
352 spatial variation of the estimated diffusion rates for 1- 8 km depth, considering the
353 sensitivity depth of surface wave to S-wave in the analysed frequency range (additional
354 file 2: [Fig. S3a](#)). The results demonstrate that the hydraulic diffusion controlling the pore
355 pressure spatially varies across the Chugoku and Shikoku region. The diffusion rates in
356 western Chugoku are generally higher than ones in the eastern area, while station with
357 the highest hydraulic diffusion is found in the eastern Shikoku. Spatial variation of
358 diffusion rate could reflect fracture density. A higher diffusion rate can be interpreted
359 that a well-developed fracture network connects to a deeper formation.

360

361 **5. Discussion**

362 **5.1 Influence of near-surface lithology**

363 The delay time of seismic velocity change to rainfall is presumably related to the near-
364 surface conditions, which influence water percolation into geological formation. The
365 time lag between rainfall events and seismic velocity changes in [Fig. 8b](#) may represent
366 the time needed for percolating rainfall to reach the water table of an unconfined
367 aquifer. Percolation through the unsaturated zone is likely determined by the
368 permeability of the near-surface layers and the surface geologic and geographic
369 conditions at the seismic station. For example, in mountain regions with high
370 permeability, water derived from the surrounding mountains percolates into
371 intermountain basins. The comparison of our result with the geological and topological
372 map of Japan ([Figs. 1b, 1c](#)) shows that stations with negative correlations are mostly

373 located in granite areas with gentle sloping topography (Fig. 1b; marked by the colour
374 pink in the legend of Fig. 1c). On the other hand, we cannot identify clear negative
375 correlation in sedimentary rocks with steep slope area in the southern Shikoku (Fig. 1b;
376 green in Fig. 1c), possibly because water flows away without percolating into deep
377 formation.

378 Because the unsaturated zone in humid climates is generally less than 10-m thick
379 (Phillips and Castro 2003), we assumed the unsaturated zone in our humid study area to
380 be shallower than 10 m. Borehole logs from the sites where our seismometers are
381 deployed classify the shallow formation as high-permeability materials and weathered
382 igneous rocks (Obara et al. 2005). Under the assumption that S-wave velocity may be
383 related to permeability, we examined plots of time lag versus S-wave velocity (Fig. 10)
384 to evaluate the relationship between lithology and time lag. Although the relationships
385 are unclear, we identified some features for each formation.

386 Among the 29 stations obtained from the step 1, the lithology of 19 stations can be
387 classified into high-permeable materials (Fig. 10a) and weathered igneous rocks (Fig.
388 10b). A total of 8 stations with high-permeability material such as sandy soil, silt, and
389 gravel shows a positive trend in which the time lag increases with increasing S-wave
390 velocity (Fig. 10a). Because the seismic velocity varies inversely with porosity, this
391 relationship confirms that percolation could be faster in more porous materials (i.e., low
392 V_s) and slower where porosity is lower.

393 In weathered igneous rocks, which consist mostly of granite, the time lag and S-wave
394 velocity show a modest negative trend (Fig. 10b). This trend may be connected to the

395 spatial concentration of fractures in these rocks. Although fractures in crystalline rocks
396 generally decrease with increasing depth, fractures are the primary determinant of
397 permeability at depths shallower than 10 m in plutonic and crystalline metamorphic
398 rocks (Freeze and Cherry 1979). Furthermore, the decreasing time lag with increasing S-
399 wave velocity implies that the water table is shallower in the less-fractured igneous
400 rocks whereas brittle, more-fractured igneous rocks allow rainfall to percolate to greater
401 depths, resulting in longer lag times for water to reach the saturated zone.

402 The estimated time lag can be also influenced by the delayed response of pore
403 pressure change associated with the diffusion mechanism. Indeed, the time lag between
404 seismic velocity change and rainfall is longer than that between groundwater level and
405 rainfall (Fig. 9). This might reflect the influence of the delayed response of pore pressure
406 change (i.e., seismic velocity change), in addition to the time delay due to percolation of
407 rainfall to the water table.

408

409 **5.2. Seismic velocity changes due to pore pressure diffusion**

410 The example shown in Fig. 11 demonstrates that pore pressure increases from July to
411 November. This pattern agrees with the seismic velocity decrease from July to
412 November. A similar pore pressure and seismic velocity variation also occurs at other
413 locations across Chugoku and Shikoku (Fig S3). It is known that rainfall in July-September
414 can trigger seasonal seismicity in the Chugoku area (Ueda et al. 2019). The similar
415 timeline suggests that the longer period seismic velocity change might have been

416 influenced by pore pressure change induced by rainfall, although the long period
417 variation is also influenced by sea level and atmospheric pressure variations.

418 The surface wave depth sensitivity to S-wave could be associated with the frequency
419 of the coda wave used to estimate seismic velocity change (Nimiya et al., 2017).
420 Although the frequency range of our seismic velocity change is sensitive to 1 – 8 km, the
421 largest sensitivity derived from velocity model in our study area seems to be within 1.5
422 – 2 km depth (see Fig. S2). Within these depths, the range of hydraulic diffusivity for
423 Chugoku and Shikoku region varies from 0.02 – 1 m²/s (Fig. 12b). Suppose we take an
424 example of 1.5 km depth, then the hydraulic diffusion rate at the western Chugoku area
425 would be 0.09-0.14 m²/s, 0.09 - 0.25 m²/s for northern Chugoku, 0.02 - 0.1 m²/s for
426 eastern Chugoku, and 0.02 - 0.5 m²/s for eastern Shikoku.

427

428 **5.3 Mechanisms of pore pressure variation**

429 We summarize our result and interpretation in Fig. 13. The near surface condition
430 (e.g., lithology and fracture) controls the percolation of rainfall, resulting in a time-lag
431 between rainfall and pore pressure increase (Fig. 13a). After the rain precipitation, we
432 expect pore pressure increase mainly due to (a) immediate loading in undrained
433 condition and (b) pore pressure diffusion.

434 As groundwater level increases due to rainfall infiltration, immediate loading causes
435 pore pressure increase from Pp1 to Pp2 in Fig. 13a, and generate thin cracks (white
436 arrow in Fig. 13b). This condition persists until pore pressure ceases to the surrounding
437 fractures in deep formation (Pp2 to Pp3 in Fig. 13a). This pore pressure variation could

438 be mainly observed by shorter period seismic velocity reduction (Fig. 6). Then, the load
439 from groundwater level increase triggers pore pressure diffusion through the pre-
440 existing fracture network. As the pore pressure front arrives (white wavy arrow in Fig.
441 13c), there is an increase of pore pressure from Pp4 to Pp5 in Fig. 13a. This pore pressure
442 increase can be monitored by longer period seismic velocity (Fig. 11).

443 We conclude that local lithology, both above the groundwater table and in the deep
444 formation, contributes to the pore pressure changes associated with rainfall. The
445 interpretations we describe here are simple ones. In real hydrogeological systems,
446 however, there are many other complex mechanisms that affect the time lag (e.g., flow
447 path influenced by geographical features), as well as the fracture permeability in the
448 deeper lithology.

449

450 **6. Conclusion**

451 The status of pore pressure changes associated with rainfall can be evaluated by
452 monitoring the seismic velocity. By calculating the cross-correlation between rainfall and
453 seismic velocity changes, we can identify the locations where seismic velocity change is
454 influenced by precipitation. Furthermore, by modelling pore pressure change based on
455 pore pressure diffusion due to rainfall, we can constrain hydraulic diffusion from long
456 period seismic velocity changes. Our primary conclusions are:

457 (1) The influence of rainfall on seismic velocity change varies depending on the
458 lithology. The clear negative correlations between rainfall and seismic
459 velocity can be observed in the granite areas and terrains with gentle

460 topography. On the contrary, there are no clear correlations observed in the
461 steep mountain areas.

462 (2) The time-lag between precipitation and seismic velocity change constrains
463 near-surface conditions that could be related to lithology-related
464 permeability. Similar time lag between precipitation and ground water level
465 demonstrates that the increased groundwater load causes a subsequent
466 decrease in seismic velocity.

467 (3) The pore pressure diffusion caused by rainfall infiltration can be modelled
468 and controls longer-term pore pressure change. The spatial variation of
469 diffusion parameter estimated by the modelling depends on fracture
470 connectivity and is spatially varied.

471

472 **Declarations**

473 **Availability of data and materials**

474 Seismic data required to evaluate the conclusions in the paper are available from NIED
475 (http://www.hinet.bosai.go.jp/about_data/?LANG=en). The meteorological data were
476 obtained from JMA (<https://www.jma.go.jp/jma/index.html>).

477

478 **Competing interests**

479 The authors declare that they have no competing interest.

480

481 **Funding**

482 This work was supported by Japan Society for the Promotion of Science grants (no.
483 JP20H01997).

484

485 **Authors' contributions**

486 RDA drafted the initial manuscript. TT proposed this study. TT, RS, and TI suggested the
487 method for the interpretation, and revised the manuscript. All authors read and
488 approved the final manuscript.

489

490 **Acknowledgements**

491 We used Hi-net seismic data from the National Research Institute for Earth Science
492 and Disaster Resilience (NIED). We obtained rainfall, sea level, and atmospheric pressure
493 data from the Japan Meteorological Agency (JMA). We appreciate Taka'aki Taira (UC
494 Berkley) for discussion, and Fernando Lawrens Hutapea (Kyushu Univ.) for his technical
495 support in computing seismic velocity change. This study was also supported by Japan
496 Society for the Promotion of Science grants (no. JP20H01997). We are grateful for the
497 support provided by the Advanced Graduate Program in Global Strategy for Green Asia
498 of Kyushu University, and International Institute for Carbon-Neutral Energy Research

499 (I2CNER) funded by the World Premier International Research Center Initiative of the
500 Ministry of Education, Culture, Sports, Science and Technology, Japan (MEXT).

501

502

503 **Figures Legends**

504 Figure 1. (a) Location map of Japan showing the study area in the Chugoku-Shikoku
505 region. (b) Topological and (c) geological maps of Chugoku and Shikoku region (modified
506 from Geological Survey of Japan AIST, 2015). The dots on the geological map represent
507 the location of seismic stations. The colour of dots in panels (b) and (c) indicates the time
508 lag shown in [Fig7c](#). Maps of the study area showing (d) seismic stations, (e) precipitation
509 gauges, and (f) ocean tidal stations, pressure gauges, and groundwater level (GWL)
510 stations. The red circle in (d-f) indicates the seismic station (N.YSHH) for which the
511 correlations in [Figs. 3,6, and 11](#) are computed. The yellow circles in (d) represent the
512 station pairs and (e) precipitation gauges within 40 km from the selected seismic station,
513 respectively.

514

515 Figure 2. Flowchart summarizing the two steps procedures to investigate the rainfall
516 influence in seismic velocity change.

517

518 Figure 3. (a) Example of unfiltered and filtered seismic velocity changes. The color of the
519 unfiltered velocity change represents the stretching correlation coefficient. (b)

520 Precipitation, (c) sea level, and (d) atmospheric pressure during the study period at the
521 station shown in Fig. 1f. (e,f) Comparisons of precipitation with changes in sea level and
522 atmospheric pressure, respectively, at the station shown in Fig. 1f. Signals are
523 normalized.

524

525 Figure 4. Pearson correlation coefficients between band-pass filtered (a) precipitation
526 and sea-level change and (b) precipitation and atmospheric pressure change at stations
527 in the study area.

528

529 Figure 5. Schematic figure of cross-correlation analysis between seismic velocity changes
530 (reference) and precipitation (shifted time series): (a) positive time lag with negative
531 correlation and (b) positive time lag with positive correlation. The delay between the
532 peaks of precipitation and seismic velocity change is represented by Δt .

533

534 Figure 6. Comparison and cross-correlation analysis between seismic velocity changes
535 and precipitation at the station shown as red dot in Fig. 1f: (a) unfiltered signals, (b)
536 band-pass filtered signals (normalized), and (c) band-pass filtered signals with
537 precipitation shifted 8 days later.

538

539 Figure 7. (a–c) Cross-correlation between seismic velocity change and precipitation at
540 the stations in the map at left, showing the estimated delay from positive time lag (solid
541 magenta line)

542

543 Figure 8. Maps of the study area showing (a) correlation coefficients between seismic
544 velocity change and precipitation at all stations after time shifting, (b) stations in (a) with
545 negative correlation coefficients < -0.2 , and (c) time delays at stations in (b). The time
546 lag in panel (c) is also shown in [Fig. 1c](#).

547

548 Figure 9. Comparison and cross-correlations between precipitation and ground water
549 level (GWL), and those between precipitation and seismic velocity. The station of this
550 example is shown in [Fig. 1f](#). (a) Relationship between unfiltered precipitation and GWL.
551 (b) Relationship between band-pass filtered precipitation and GWL. (c) Relationship
552 between band-pass filtered precipitation and GWL with precipitation shifted earlier by
553 5 days. (d) The relationship between band-pass filtered precipitation and seismic
554 velocity change (normalized) with precipitation shifted earlier by 9 days.

555

556 Figure 10. S-wave velocity versus time delays of precipitation in (a) high-permeability
557 materials and (b) weathered igneous rocks.

558

559 Figure 11. Comparison of moving averaged seismic velocity changes and pore pressure
560 estimated from precipitation at the seismic station (red dots in [Fig. 1f](#)). (a) Moving
561 averaged seismic velocity change. (b) Precipitation and the calculated pore pressure
562 change. (c) Correlation between averaged seismic velocity change and pore pressure.
563 The signals are normalized.

564

565 Figure 12. (a) The correlation map between seismic velocity change and pore pressure.
566 (b) The map of diffusion parameter for each depth (1, 1.5, 2, 4, 6, and 8km). The stations
567 with negative correlations smaller than 0.2 are not included on the map. The colorbar in
568 each panel represents the different range of hydraulic diffusion rate.

569

570 Figure 13. The summary of the mechanism crustal pore pressure change (P_p) associated
571 with rainfall (modified from Talwani et al., 1997). (a) The time duration for the
572 immediate high pore pressure (due to undrained effect) and pore pressure diffusion to
573 occur with the increasing water level. The schematic figures of (b) immediate loading
574 and (c) pore pressure diffusion in a later time. The white arrow in (b) represents the
575 immediate increase of pore pressure due to undrained condition. The white wavy
576 arrows in (c) represent the pore pressure diffusion.

577

578

579 **References**

580 Aizen EM, Aizen VB, Melack JM, et al (2001) Precipitation and atmospheric circulation
581 patterns at mid-latitudes of Asia. *Int J Climatol* 21:535–556.

582 <https://doi.org/10.1002/joc.626>

583 Albino F, Amelung F, Gregg P (2018) The Role of Pore Fluid Pressure on the Failure of
584 Magma Reservoirs: Insights From Indonesian and Aleutian Arc Volcanoes. *J*

585 *Geophys Res Solid Earth* 123:1328-1349. <https://doi.org/10.1002/2017JB014523>

586 [Aoi, S., Asano, Y., Kunugi, T. et al. MOWLAS: NIED observation network for earthquake,](#)
587 [tsunami and volcano. Earth Planets Space 72, 126 \(2020\).](#)
588 <https://doi.org/10.1186/s40623-020-01250-x>

589 Ben-Zion Y, Leary P (1986) Thermoelastic strain in a half-space covered by
590 unconsolidated material. Bull Seismol Soc Am. 76:1447-1460

591 Berger J (1975) A note on thermoelastic strains and tilts. J Geophys Res 80:274–277.
592 <https://doi.org/10.1029/jb080i002p00274>

593 Bettinelli P, Avouac JP, Flouzat M, et al (2008) Seasonal variations of seismicity and
594 geodetic strain in the Himalaya induced by surface hydrology. Earth Planet Sci
595 Lett. 266: 332-244. <https://doi.org/10.1016/j.epsl.2007.11.021>

596 Bièvre G, Franz M, Larose E, et al (2018) Influence of environmental parameters on the
597 seismic velocity changes in a clayey mudflow (Pont-Bourquin Landslide,
598 Switzerland). Engineering Geology 245:248–257.
599 <https://doi.org/10.1016/j.enggeo.2018.08.013>

600 Chaves EJ, Schwartz SY (2016) Monitoring transient changes within overpressured
601 regions of subduction zones using ambient seismic noise. Sci Adv 2:e1501289.
602 <https://doi.org/10.1126/sciadv.1501289>

603 Ellsworth WL (2013) Injection-Induced Earthquakes. Science 341:1225942–1225942.
604 <https://doi.org/10.1126/science.1225942>

605 Freeze, R.A., Cherry, J.A. (1979) Groundwater. Prentice-Hall, Inc., Englewood, Cliffs, N.J.
606 07632.

607 Gassenmeier M, Sens-Schönfelder C, Delatre M, Korn M (2015) Monitoring of
608 environmental influences on seismic velocity at the geological storage site for CO₂
609 in Ketzin (Germany) with ambient seismic noise. *Geophys J Int* 200:524–533.
610 <https://doi.org/10.1093/gji/ggu413>

611 Geological Survey of Japan, AIS (ed.). (2015) Seamless digital geological map of Japan
612 1:200,000. May 29, 2015 version. Geological Survey of Japan, National Institute of
613 Advanced Industrial Science and Technology. <https://gbank.gsj.jp/geonavi/>
614 (accessed 10 February 2020).

615 Grêt A, Snieder R, Scales J (2006) Time-lapse monitoring of rock properties with coda
616 wave interferometry. *J Geophys Res Solid Earth* 111(3):1-11.
617 <https://doi.org/10.1029/2004JB003354>

618 Hadziioannou C, Larose E, Coutant O, et al (2009) Stability of monitoring weak changes
619 in multiply scattering media with ambient noise correlation: Laboratory
620 experiments. *J Acoust Soc Am.* 125:3688–3695.
621 <https://doi.org/10.1121/1.3125345>

622 Hainzl S, Kraft T, Wassermann J, et al (2006) Evidence for rainfall-triggered earthquake
623 activity. *Geophys Res Lett* 33: L19303. <https://doi.org/10.1029/2006GL027642>

624 Heki K (2004) Dense GPS array as a new sensor of seasonal changes of surface loads.
625 In: Sparks RSJ, Hawkesworth CJ (eds) *Geophysical Monograph Series*. American
626 Geophysical Union, Washington, D.C., pp 177 – 196

627 Hillers G, Ben-Zion Y, Campillo M, Zigone D (2015) Seasonal variations of seismic

628 velocities in the San Jacinto fault area observed with ambient seismic noise.
629 Geophys J Int 202:920–932. <https://doi.org/10.1093/gji/ggv151>

630 Hillers G, Graham N, Campillo M, et al (2012) Global oceanic microseism sources as
631 seen by seismic arrays and predicted by wave action models. *Geochemistry,*
632 *Geophys Geosystems* 13: Q01021. <https://doi.org/10.1029/2011GC003875>

633 Hutapea FL, Tsuji T, Ikeda T (2020) Real-time crustal monitoring system of Japanese
634 Islands based on spatio-temporal seismic velocity variation. *Earth, Planets Sp*
635 *72:19*. <https://doi.org/10.1186/s40623-020-1147-y>

636 Ikeda T, Tsuji T (2018) Temporal change in seismic velocity associated with an offshore
637 MW 5.9 Off-Mie earthquake in the Nankai subduction zone from ambient noise
638 cross-correlation. *Prog Earth Planet Sci* 5:62. [https://doi.org/10.1186/s40645-018-](https://doi.org/10.1186/s40645-018-0211-8)
639 [0211-8](https://doi.org/10.1186/s40645-018-0211-8)

640 Ikeda T, Tsuji T, Nakatsukasa M, et al (2018) Imaging and monitoring of the shallow
641 subsurface using spatially windowed surface-wave analysis with a single
642 permanent seismic source. *Geophysics* 83: EN23–EN38.
643 <https://doi.org/10.1190/geo2018-0084.1>

644 Kraft T, Wassermann J, Schmedes E, Igel H (2006) Meteorological triggering of
645 earthquake swarms at Mt. Hochstaufen, SE-Germany. *Tectonophysics* 424:245–
646 258. <https://doi.org/10.1016/j.tecto.2006.03.044>

647 Meier U, Shapiro NM, Brenguier F (2010) Detecting seasonal variations in seismic
648 velocities within Los Angeles basin from correlations of ambient seismic noise.

649 Geophys J Int 181:985–996. <https://doi.org/10.1111/j.1365-246X.2010.04550.x>

650 Miao Y, Shi Y, Wang SY (2018) Temporal change of near-surface shear wave velocity
651 associated with rainfall in Northeast Honshu, Japan. *Earth, Planets Sp* 70:204.
652 <https://doi.org/10.1186/s40623-018-0969-3>

653 Minato S, Tsuji T, Ohmi S, Matsuoka T (2012) Monitoring seismic velocity change
654 caused by the 2011 Tohoku-oki earthquake using ambient noise records. *Geophys*
655 *Res Lett* 39: L09309. <https://doi.org/10.1029/2012GL051405>

656 Mordret A, Mikesell TD, Harig C, et al (2016) Monitoring southwest Greenland’s ice
657 sheet melt with ambient seismic noise. *Sci Adv* 2:e1501538.
658 <https://doi.org/10.1126/sciadv.1501538>

659 Nakata N, Chang JP, Lawrence JF, Boué P (2015) Body wave extraction and tomography
660 at Long Beach, California, with ambient-noise interferometry. *J Geophys Res Solid*
661 *Earth* 120:1159–1173. <https://doi.org/10.1002/2015JB011870>

662 Nakata N, Snieder R (2012) Estimating near-surface shear wave velocities in Japan by
663 applying seismic interferometry to KiK-net data. *J Geophys Res Solid Earth* 117:
664 B01308. <https://doi.org/10.1029/2011JB008595>

665 Nakata N, Snieder R, Tsuji T, et al (2011) Shear wave imaging from traffic noise using
666 seismic interferometry by cross-coherence. *Geophysics* 76:SA97–SA106.
667 <https://doi.org/10.1190/geo2010-0188.1>

668 Nimiya H, Ikeda T, Tsuji T (2017) Spatial and temporal seismic velocity changes on
669 Kyushu Island during the 2016 Kumamoto earthquake. *Sci Adv* 3:e1700813.

670 <https://doi.org/10.1126/sciadv.1700813>

671 Nishida K, Kawakatsu H, Obara K (2008) Three-dimensional crustal S wave velocity
672 structure in Japan using microseismic data recorded by Hi-net tiltmeters. Journal
673 of Geophysical Research: Solid Earth 113. <https://doi.org/10.1029/2007JB005395>

674 Niu F, Silver PG, Daley TM, et al (2008) Preseismic velocity changes observed from
675 active source monitoring at the Parkfield SAFOD drill site. Nature 454:204–208.
676 <https://doi.org/10.1038/nature07111>

677 Obara K, Kasahara K, Hori S, Okada Y (2005) A densely distributed high-sensitivity
678 seismograph network in Japan:Hi-net by National Research Institute for Earth
679 Science and Disaster Prevention. Rev Sci Instrum 76:21301.
680 <https://doi.org/10.1063/1.1854197>

681 Phillips FM, Castro MC (2003) 5.15 - Groundwater Dating and Residence-time
682 Measurements. In: Holland HD, Turekian, K.K. (Eds.), Treatise on Geochemistry.
683 Elsevier, Oxford,, pp 451–497. <https://doi.org/10.1016/B0-08-043751-6/05136-7>

684 Prawirodirdjo L, Ben-Zion Y, Bock Y (2006) Observation and modeling of thermoelastic
685 strain in Southern California Integrated GPS Network daily position time series. J
686 Geophys Res Solid Earth 111:1–10. <https://doi.org/10.1029/2005JB003716>

687 Richter T, Sens-Schönfelder C, Kind R, Asch G (2014) Comprehensive observation and
688 modeling of earthquake and temperature-related seismic velocity changes in
689 northern Chile with passive image interferometry. J Geophys Res Solid Earth
690 119:4747–4765. <https://doi.org/10.1002/2013JB010695>

691 Rivet D, Brenguier F, Cappa F (2015) Improved detection of preeruptive seismic
692 velocity drops at the Piton de La Fournaise volcano. *Geophys Res Lett* 42:6332–
693 6339. <https://doi.org/10.1002/2015GL064835>

694 Sato T, Fukuda Y, Aoyama Y, et al (2001) On the observed annual gravity variation and
695 the effect of sea surface height variations. *Phys Earth Planet Inter* 123:45–63.
696 [https://doi.org/10.1016/S0031-9201\(00\)00216-8](https://doi.org/10.1016/S0031-9201(00)00216-8)

697 Saito M (1988) DISPER80: A subroutine package for the calculation of seismic normal
698 mode solutions. *Seismological Algorithms: Computational Methods and Computer*
699 *Programs* 293–319.

700 Sens-Schönfelder C, Eulenfeld T (2019) Probing the in situ Elastic Nonlinearity of Rocks
701 with Earth Tides and Seismic Noise. *Phys Rev Lett* 122:138501.
702 <https://doi.org/10.1103/PhysRevLett.122.138501>

703 Sens-Schönfelder C, Wegler U (2006) Passive image interferometry and seasonal
704 variations of seismic velocities at Merapi Volcano, Indonesia. *Geophys Res Lett*
705 33:1–5. <https://doi.org/10.1029/2006GL027797>

706 Silver PG, Daley TM, Niu F, Majer EL (2007) Active source monitoring of cross-well
707 seismic travel time for stress-induced changes. *Bull Seismol Soc Am* 97:281–293.
708 <https://doi.org/10.1785/0120060120>

709 Taira T, Brenguier F (2016) Response of hydrothermal system to stress transients at
710 Lassen Volcanic Center, California, inferred from seismic interferometry with
711 ambient noise. *Earth, Planets Sp* 68:162. [33](https://doi.org/10.1186/s40623-016-</p></div><div data-bbox=)

712 0538-6

713 Takano T, Nishimura T, Nakahara H (2017) Seismic velocity changes concentrated at
714 the shallow structure as inferred from correlation analyses of ambient noise
715 during volcano deformation at Izu-Oshima, Japan. J Geophys Res Solid Earth
716 122:6721–6736. <https://doi.org/10.1002/2017JB014340>

717 Talwani P (1997) On the Nature of Reservoir-induced Seismicity. Pure appl geophys
718 150:473–492. <https://doi.org/10.1007/s000240050089>

719 Talwani P, Chen L, Gahalaut K (2007) Seismogenic permeability, ks. Journal of
720 Geophysical Research: Solid Earth 112: <https://doi.org/10.1029/2006JB004665>

721 Tsai VC (2011) A model for seasonal changes in GPS positions and seismic wave speeds
722 due to thermoelastic and hydrologic variations. J Geophys Res 116:B04404.
723 <https://doi.org/10.1029/2010JB008156>

724 Tsuji T, Tokuyama H, Costa Pisani P, Moore G (2008) Effective stress and pore pressure
725 in the Nankai accretionary prism off the Muroto Peninsula, southwestern Japan. J
726 Geophys Res 113:B11401. <https://doi.org/10.1029/2007JB005002>.

727 Tsuji T, Johansen TA, Ruud BO, Ikeda T, Matsuoka T (2012), Surface-wave analysis for
728 identifying unfrozen zones in subglacial sediments, GEOPHYSICS, 77, EN17-EN27,
729 doi:10.1190/geo2011-0222.1.

730 Tsuji T, Kamei R, Pratt G (2014), Pore pressure distribution of a mega-splay fault system
731 in the Nankai Trough subduction zone: Insight into up-dip extent of the
732 seismogenic zone, Earth and Planetary Science Letters, 396, 165-178,

733 doi:10.1016/j.epsl.2014.04.011.

734 Ueda H, Kozono T, Fujita E, et al (2013) Crustal deformation associated with the 2011
735 Shinmoe-dake eruption as observed by tiltmeters and GPS. Earth, Planets Sp
736 65:517–525. <https://doi.org/10.5047/eps.2013.03.001>

737 Ueda T, Kato A (2019) Seasonal Variations in Crustal Seismicity in San-in District,
738 Southwest Japan. Geophysical Research Letters 46:3172–3179.
739 <https://doi.org/10.1029/2018GL081789>

740 Wang Q-Y, Brenguier F, Campillo M, et al (2017) Seasonal Crustal Seismic Velocity
741 Changes Throughout Japan. J Geophys Res Solid Earth 122:7987–8002.
742 <https://doi.org/10.1002/2017JB014307>

743 Yamamura K, Sano O, Utada H, et al (2003) Long-term observation of in situ seismic
744 velocity and attenuation. J Geophys Res Solid Earth 108(B6):2317.
745 <https://doi.org/10.1029/2002JB002005>

746 Yukutake Y, Ueno T, Miyaoka K (2016) Determination of temporal changes in seismic
747 velocity caused by volcanic activity in and around Hakone volcano, central Japan,
748 using ambient seismic noise records. Prog Earth Planet Sci 3:29.
749 <https://doi.org/10.1186/s40645-016-0106-5>

Figures

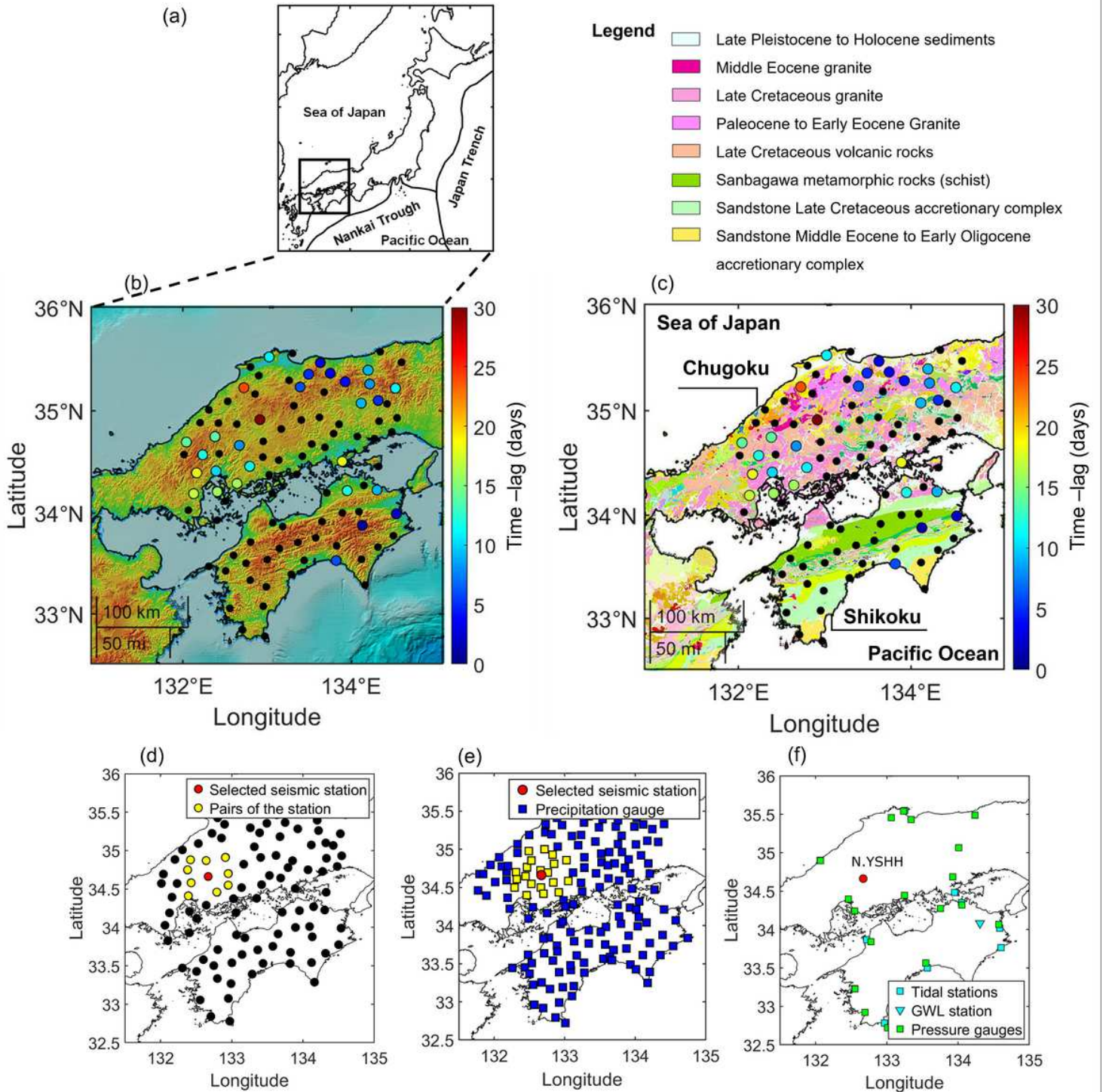


Figure 1

(a) Location map of Japan showing the study area in the Chugoku-Shikoku region. (b) Topological and (c) geological maps of Chugoku and Shikoku region (modified from Geological Survey of Japan AIST, 2015). The dots on the geological map represent the location of seismic stations. The colour of dots in panels (b) and (c) indicates the time lag shown in Fig7c. Maps of the study area showing (d) seismic

stations, (e) precipitation gauges, and (f) ocean tidal stations, pressure gauges, and groundwater level (GWL) stations. The red circle in (d-f) indicates the seismic station (N.YSHH) for which the correlations in Figs. 3,6, and 11 are computed. The yellow circles in (d) represent the station pairs and (e) precipitation gauges within 40 km from the selected seismic station, respectively.

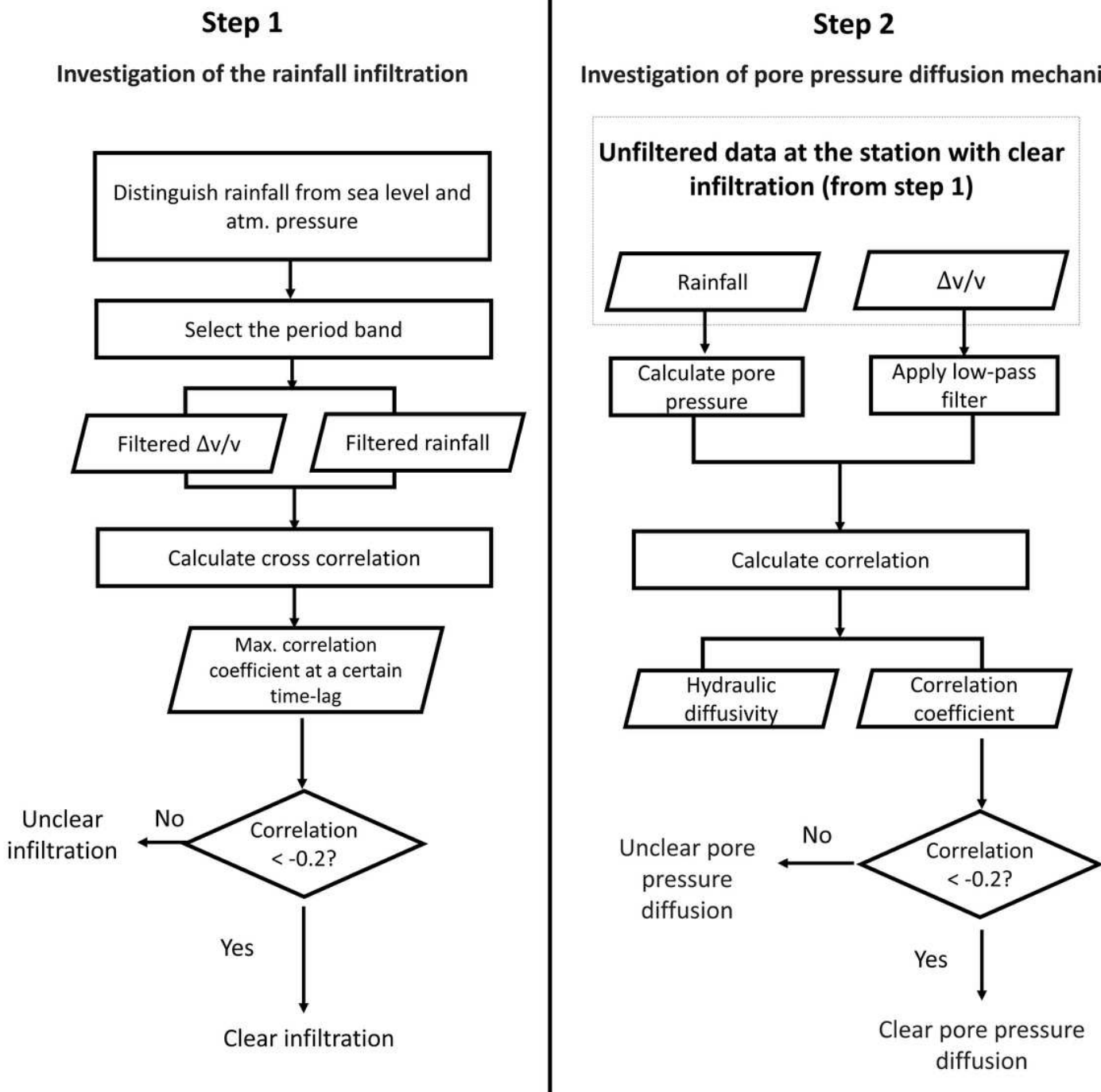


Figure 2

Flowchart summarizing the two steps procedures to investigate the rainfall influence in seismic velocity change.

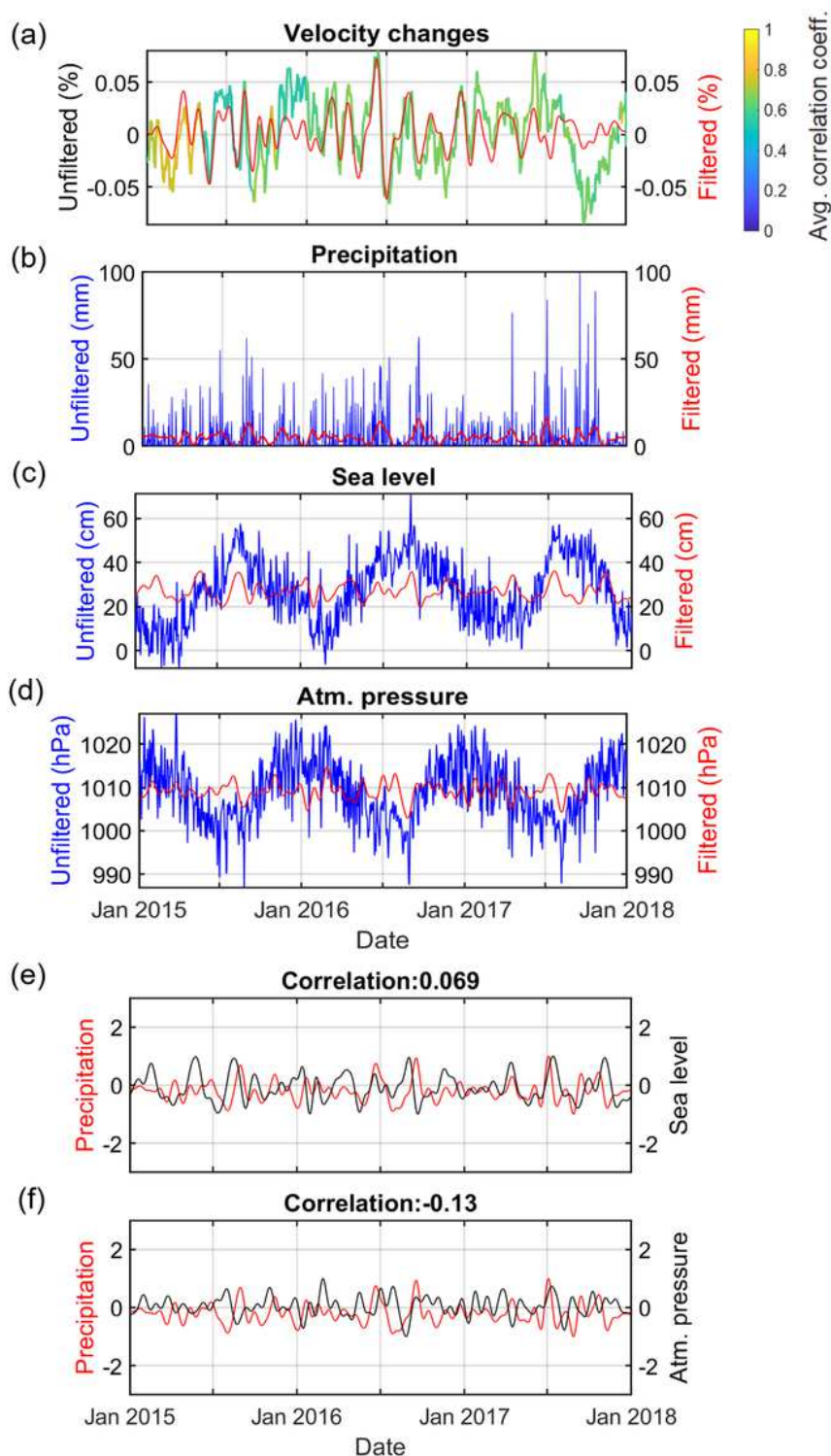


Figure 3

(a) Example of unfiltered and filtered seismic velocity changes. The color of the unfiltered velocity change represents the stretching correlation coefficient. (b) Precipitation, (c) sea level, and (d) atmospheric pressure during the study period at the station shown in Fig. 1f. (e,f) Comparisons of precipitation with changes in sea level and atmospheric pressure, respectively, at the station shown in Fig. 1f. Signals are normalized.

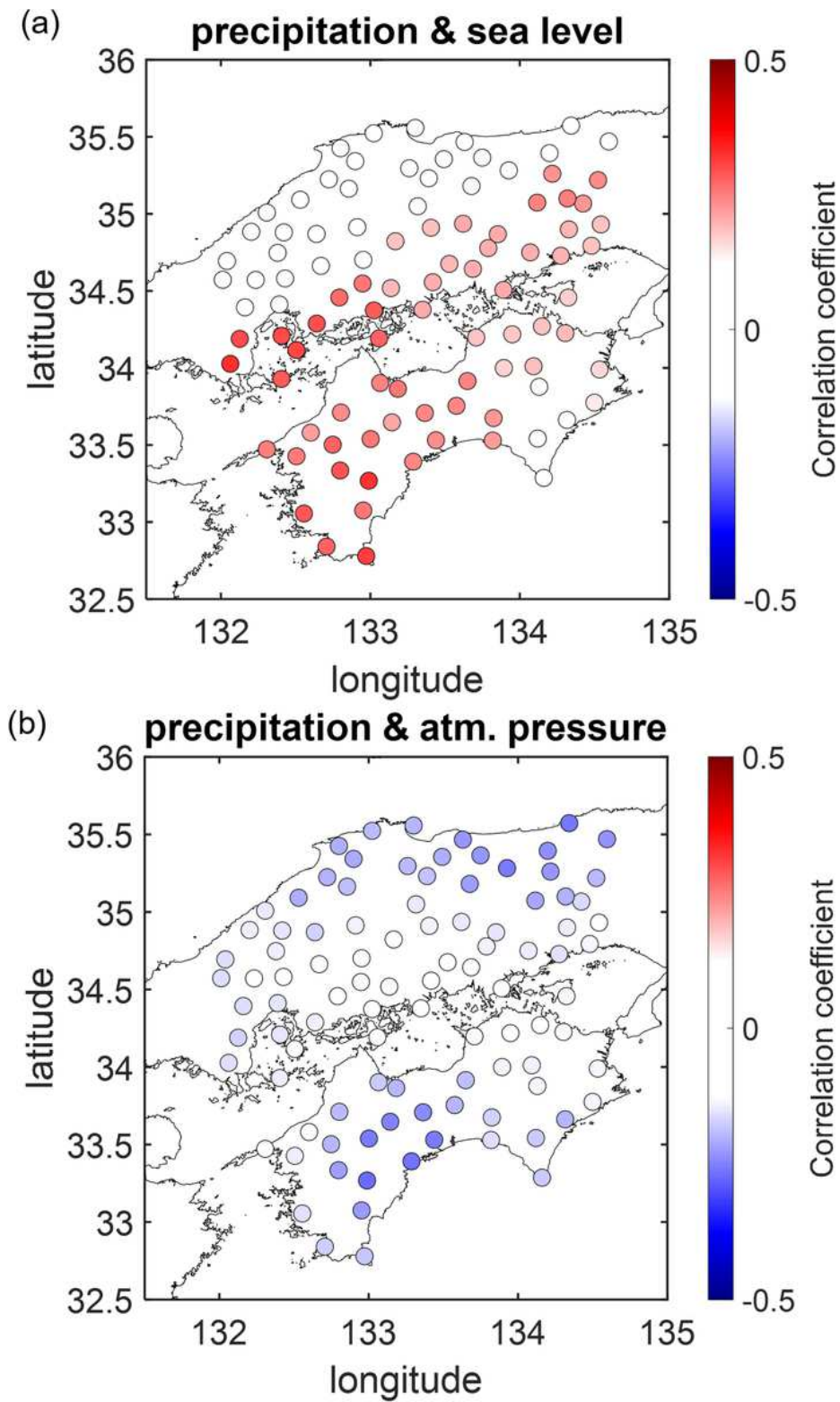
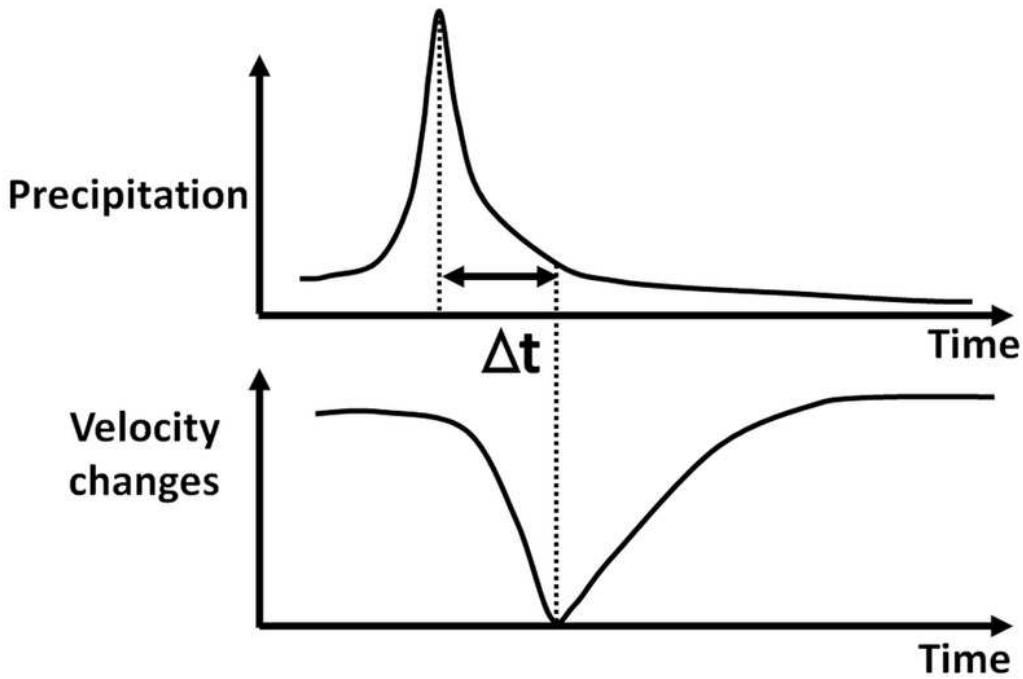


Figure 4

Pearson correlation coefficients between band-pass filtered (a) precipitation and sea-level change and (b) precipitation and atmospheric pressure change at stations in the study area.

(a) Positive lag – negative correlation



(b) Positive lag – positive correlation

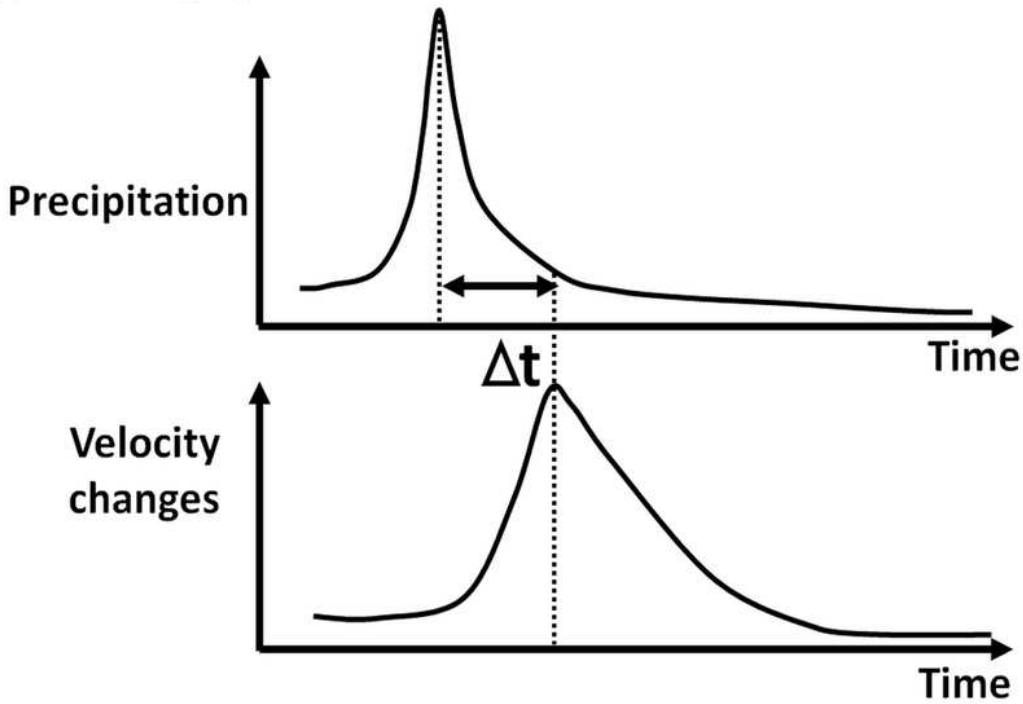
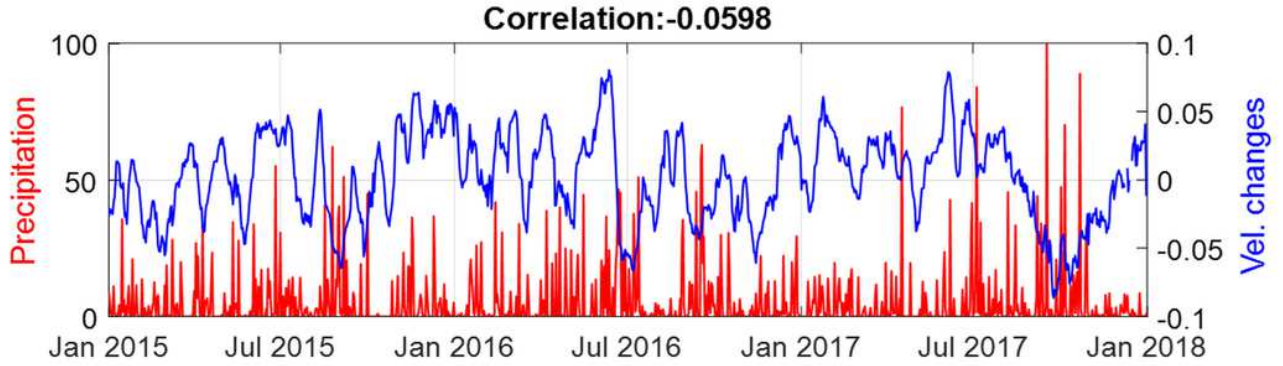


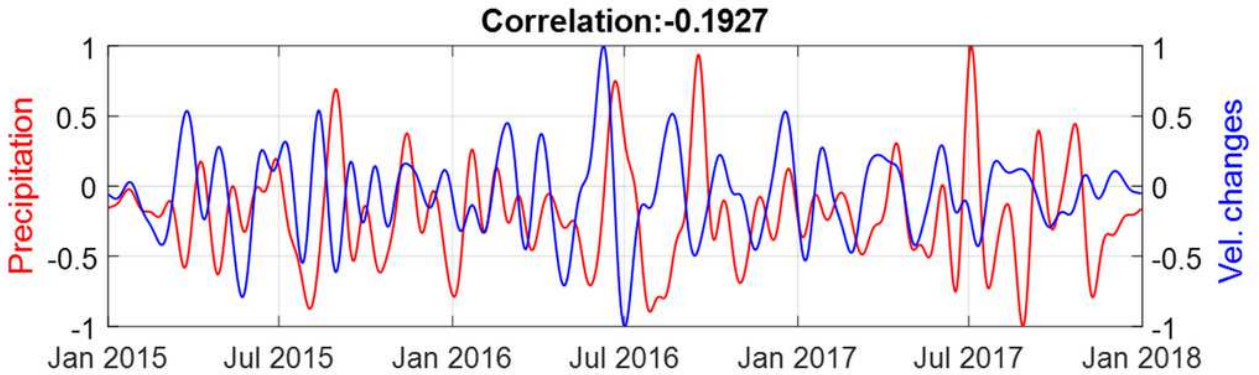
Figure 5

Schematic figure of cross-correlation analysis between seismic velocity changes (reference) and precipitation (shifted time series): (a) positive time lag with negative correlation and (b) positive time lag with positive correlation. The delay between the peaks of precipitation and seismic velocity change is represented by Δt .

(a) Without bandpass filter



(b) With bandpass filter



(c) With bandpass filter and time-shift

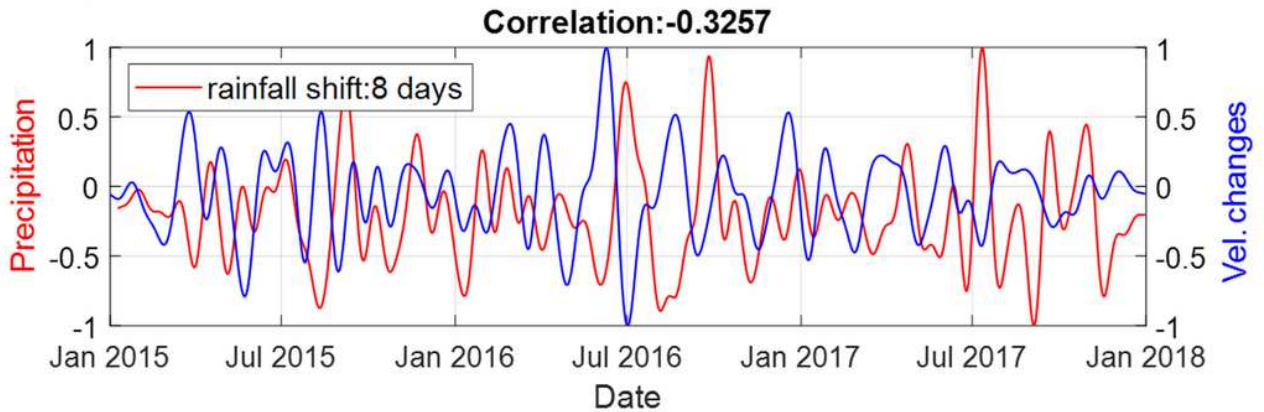


Figure 6

Comparison and cross-correlation analysis between seismic velocity changes and precipitation at the station shown as red dot in Fig. 1f: (a) unfiltered signals, (b) band-pass filtered signals (normalized), and (c) band-pass filtered signals with precipitation shifted 8 days later.

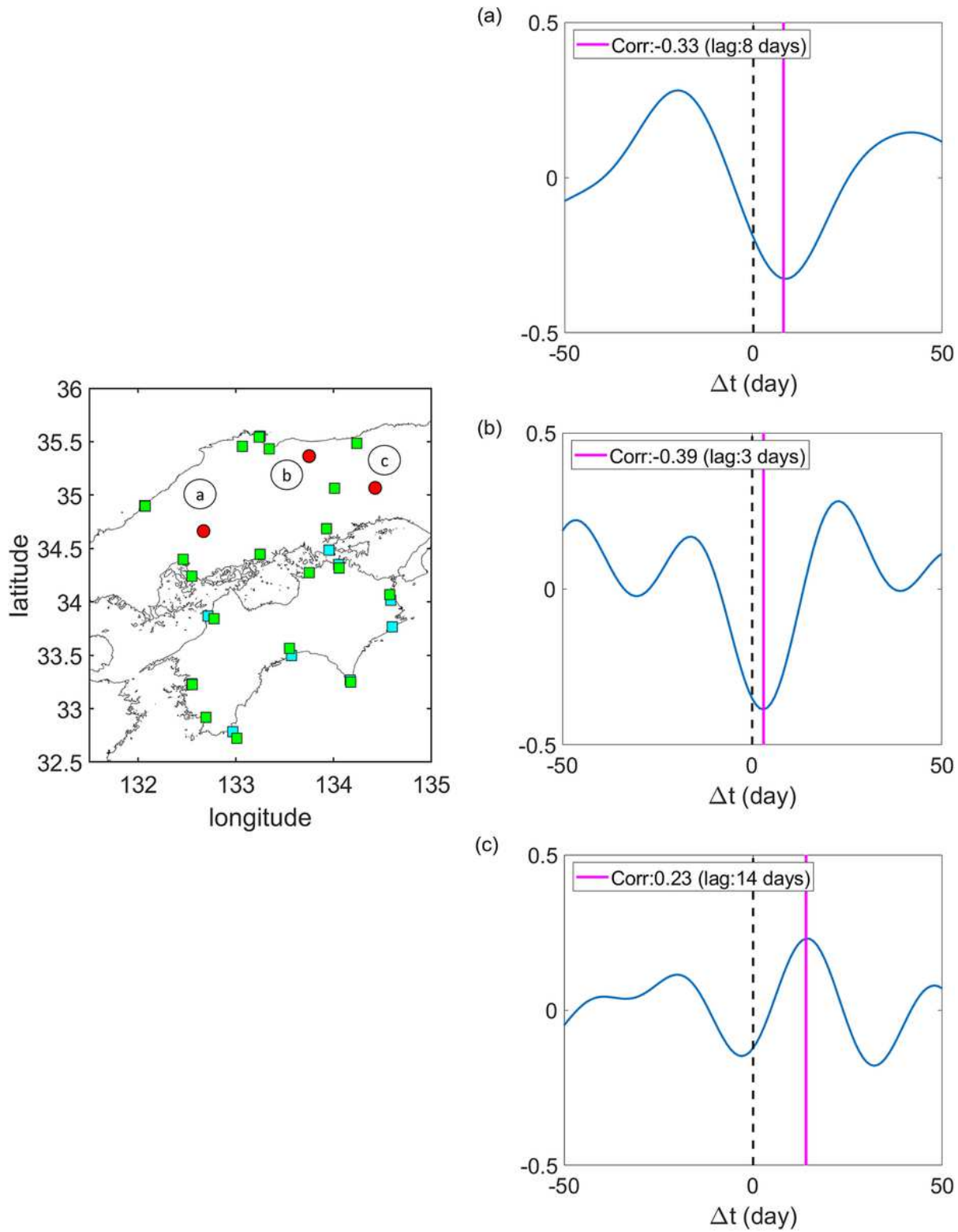


Figure 7

(a–c) Cross-correlation between seismic velocity change and precipitation at the stations in the map at left, showing the estimated delay from positive time lag (solid magenta line)

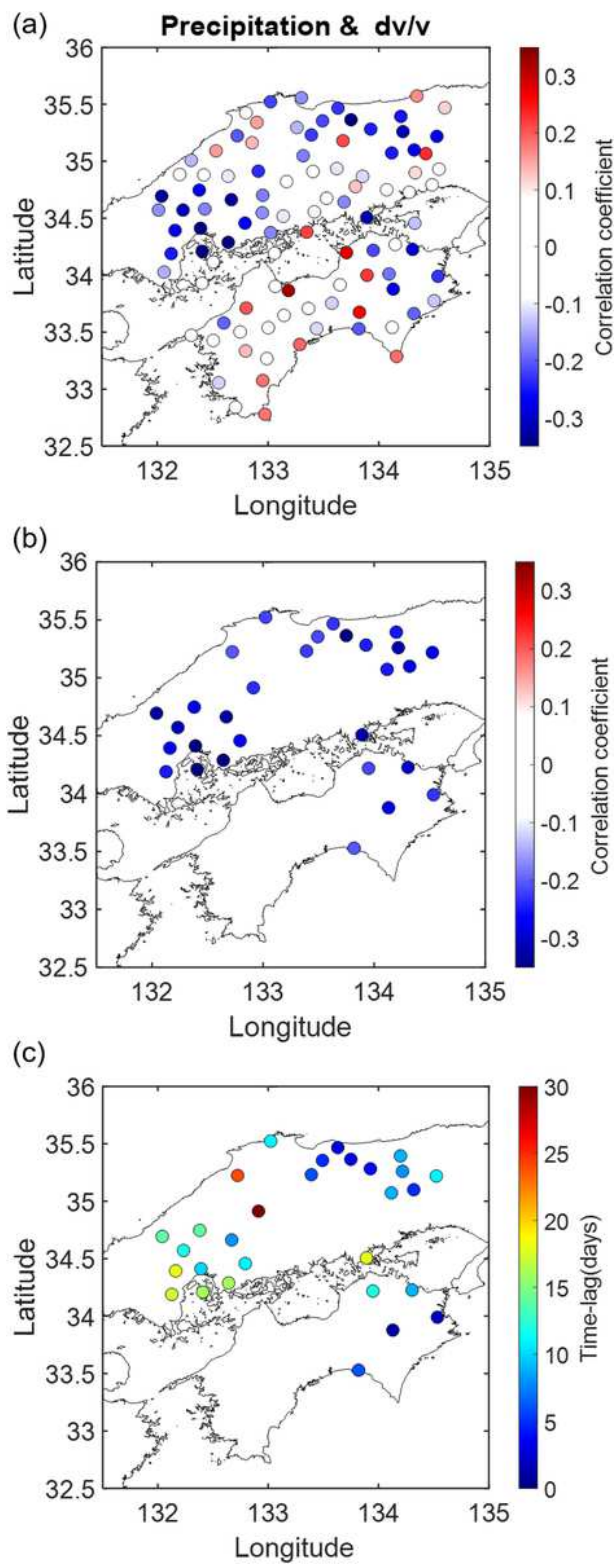


Figure 8

Maps of the study area showing (a) correlation coefficients between seismic velocity change and precipitation at all stations after time shifting, (b) stations in (a) with negative correlation coefficients < -0.2 , and (c) time delays at stations in (b). The time lag in panel (c) is also shown in Fig. 1c.

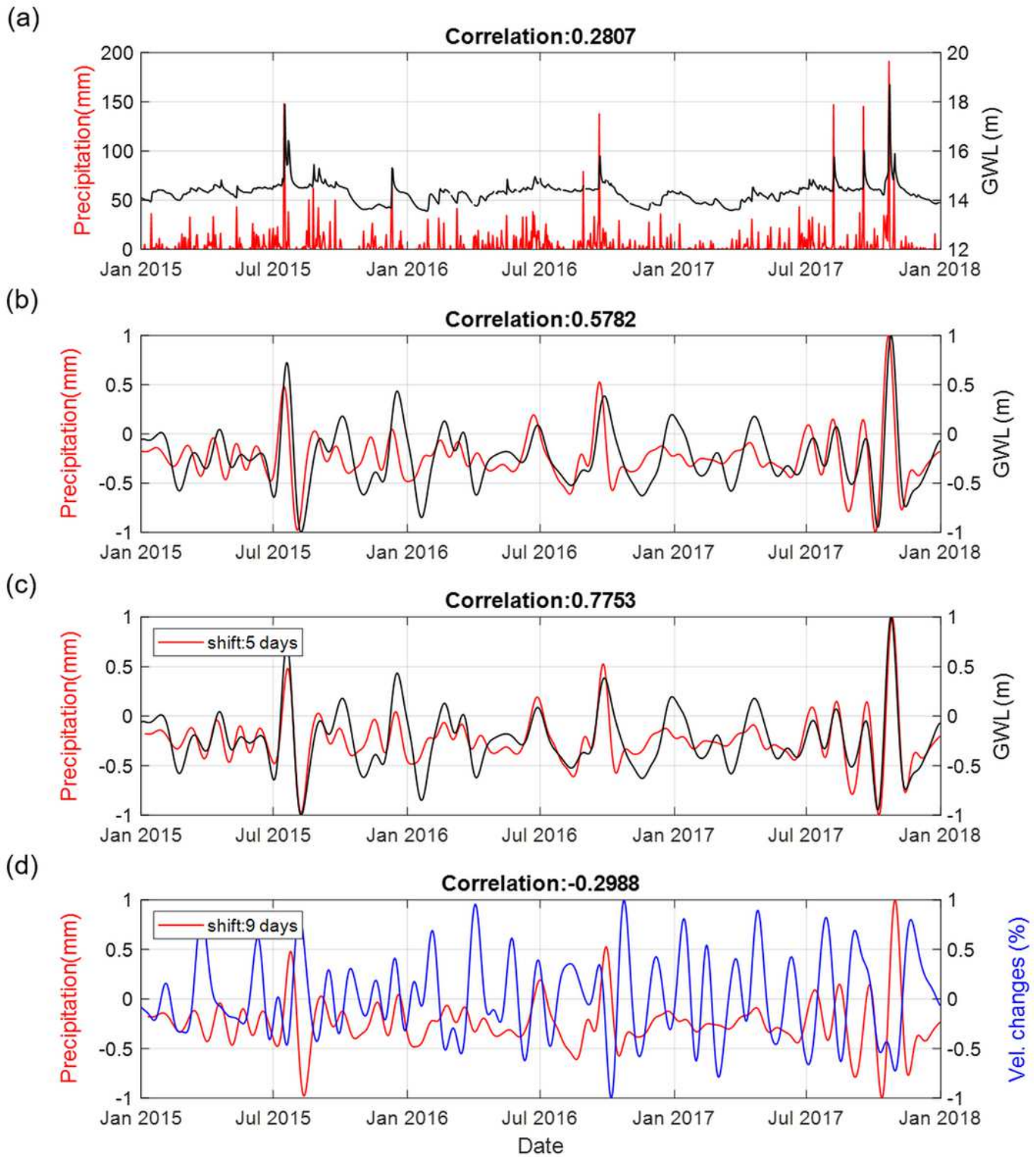
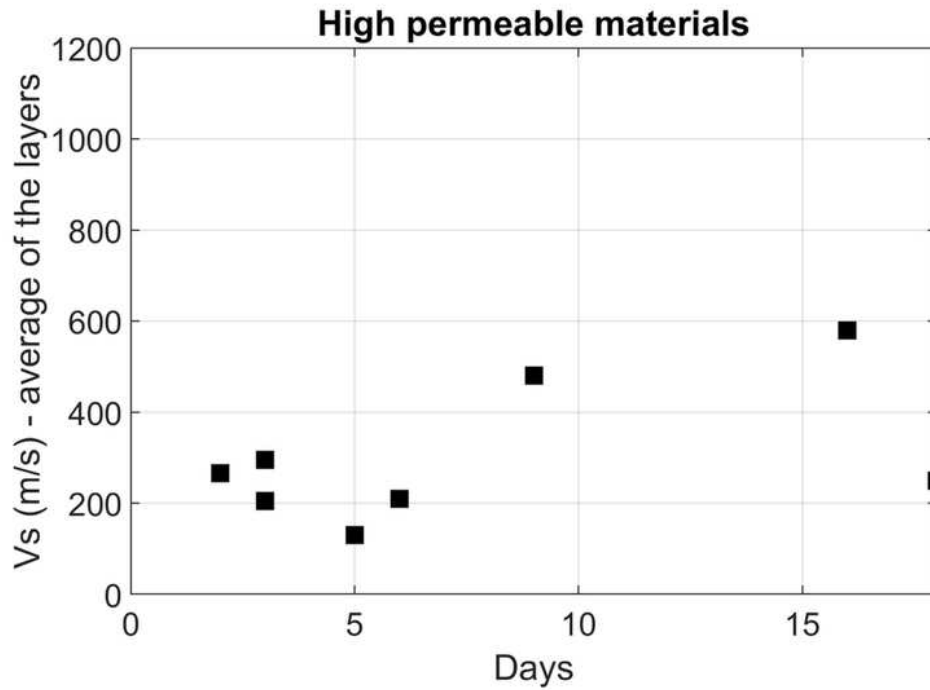


Figure 9

Comparison and cross-correlations between precipitation and ground water level (GWL), and those between precipitation and seismic velocity. The station of this example is shown in Fig. 1f. (a) Relationship between unfiltered precipitation and GWL. (b) Relationship between band-pass filtered precipitation and GWL. (c) Relationship between band-pass filtered precipitation and GWL with

precipitation shifted earlier by 5 days. (d) The relationship between band-pass filtered precipitation and seismic velocity change (normalized) with precipitation shifted earlier by 9 days.

(a)



(b)

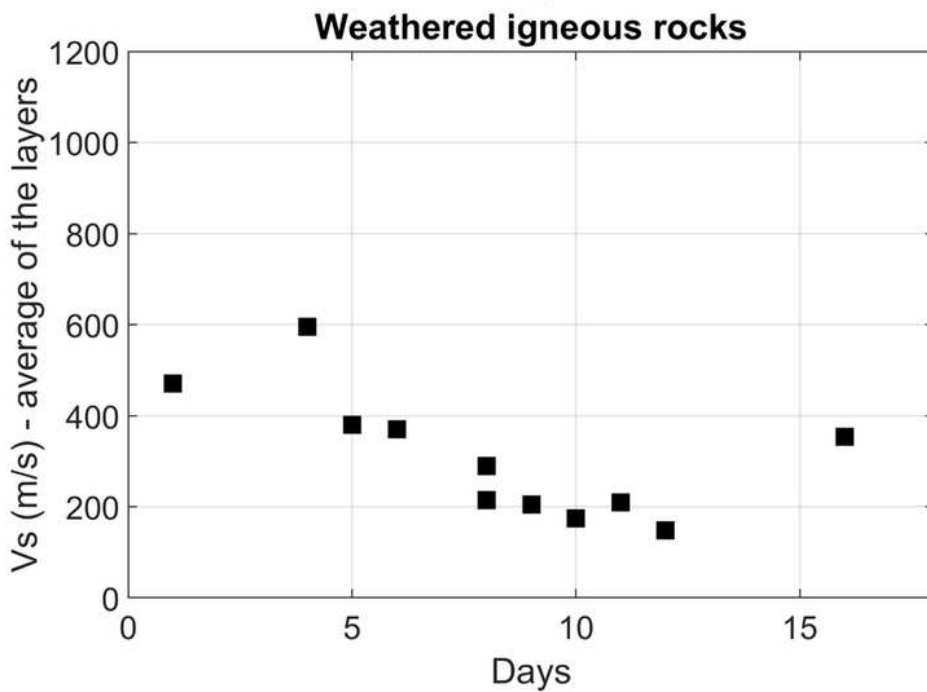
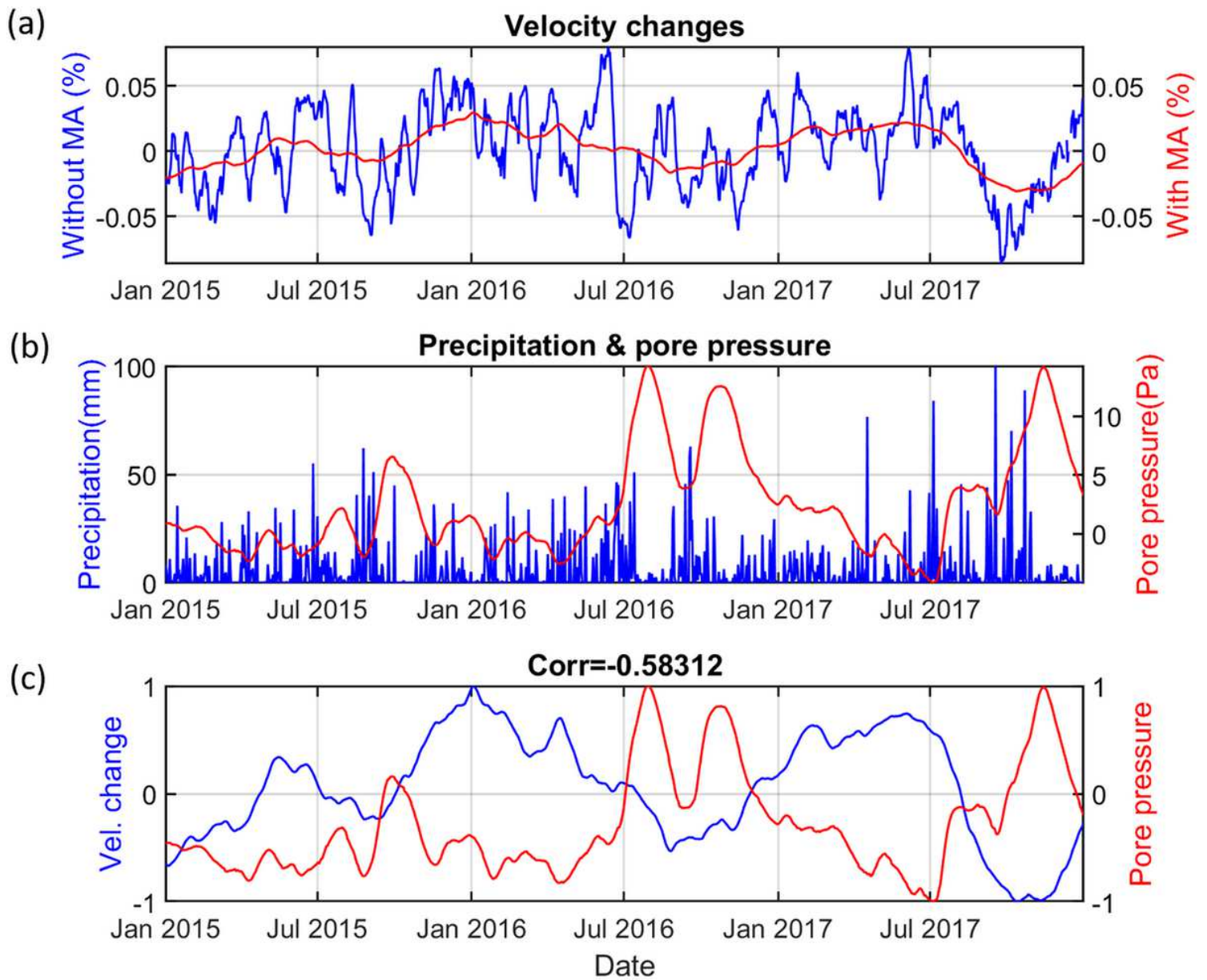


Figure 10

S-wave velocity versus time delays of precipitation in (a) high-permeability materials and (b) weathered igneous rocks.



Parameter of pore pressure calculation

Diffusion rate: $0.14 \text{ m}^2/\text{s}$

Depth: 1.5 km

Figure 11

Comparison of moving averaged seismic velocity changes and pore pressure estimated from precipitation at the seismic station (red dots in Fig. 1f). (a) Moving averaged seismic velocity change. (b) Precipitation and the calculated pore pressure change. (c) Correlation between averaged seismic velocity change and pore pressure. The signals are normalized.

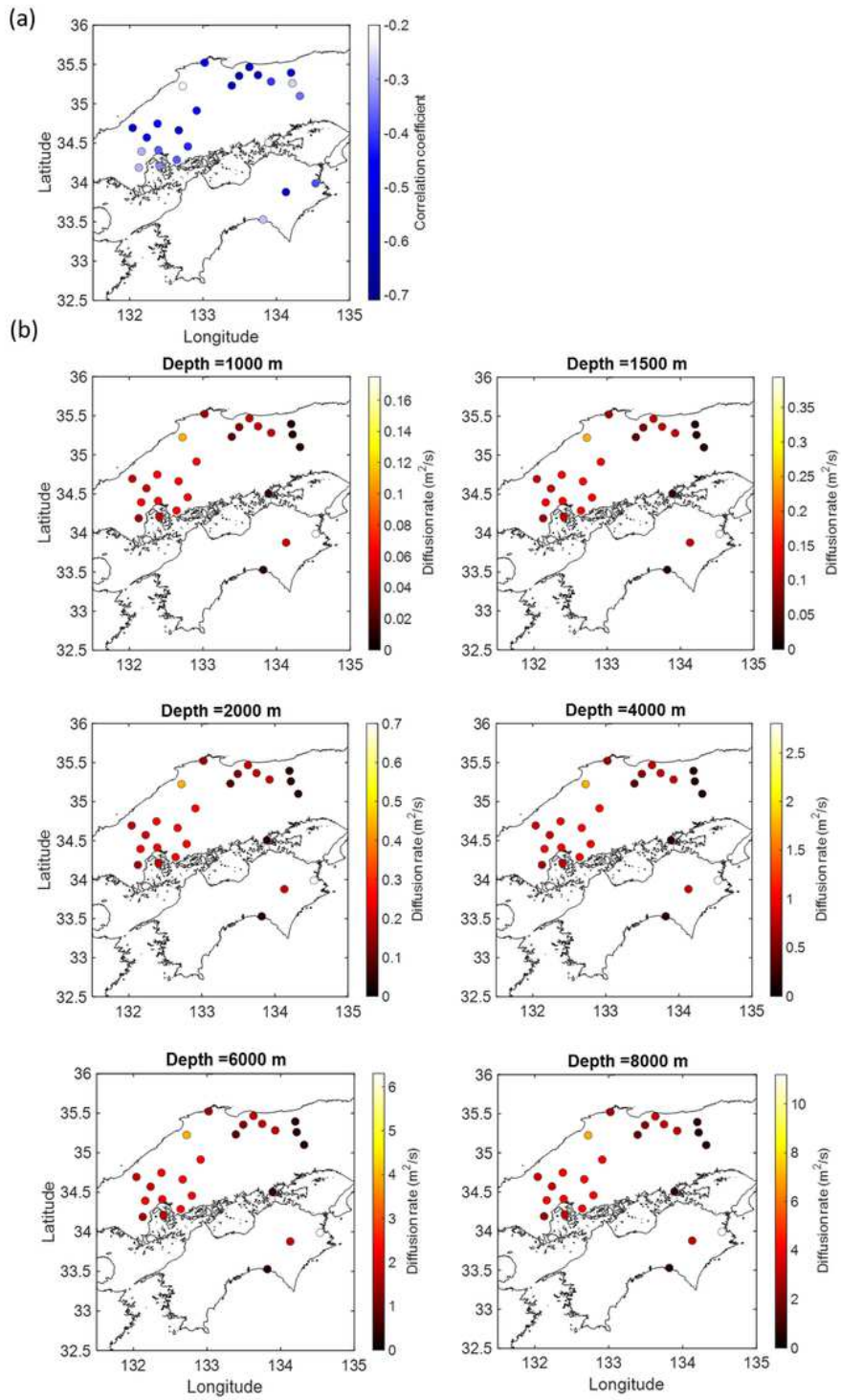


Figure 12

(a) The correlation map between seismic velocity change and pore pressure. (b) The map of diffusion parameter for each depth (1, 1.5, 2, 4, 6, and 8km). The stations with negative correlations smaller than 0.2 are not included on the map. The colorbar in each panel represents the different range of hydraulic diffusion rate.

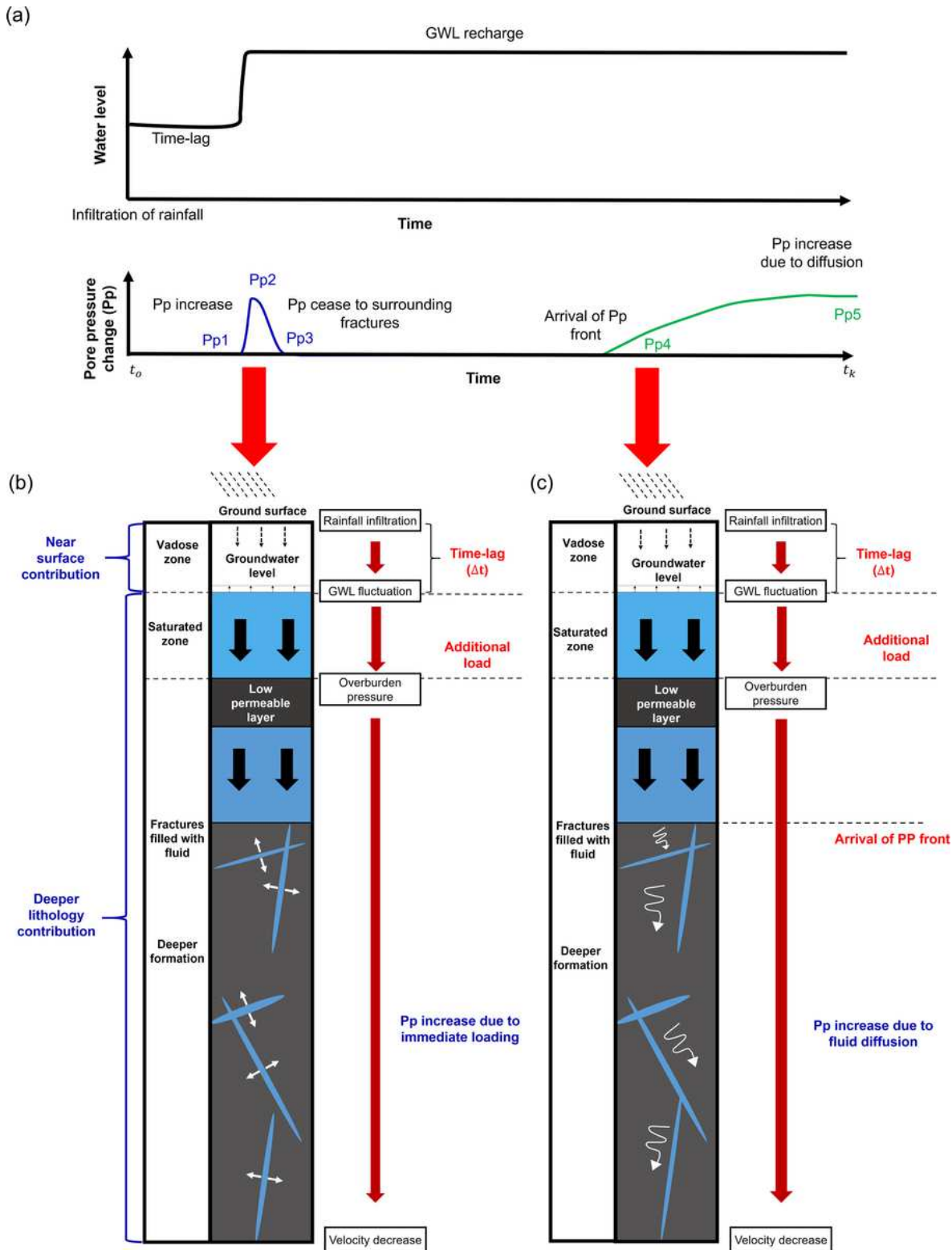


Figure 13

The summary of the mechanism crustal pore pressure change (Pp) associated with rainfall (modified from Talwani et al., 1997). (a) The time duration for the immediate high pore pressure (due to undrained effect) and pore pressure diffusion to occur with the increasing water level. The schematic figures of (b) immediate loading and (c) pore pressure diffusion in a later time. The white arrow in (b) represents the

immediate increase of pore pressure due to undrained condition. The white wavy arrows in (c) represent the pore pressure diffusion.

Supplementary Files

This is a list of supplementary files associated with this preprint. Click to download.

- [SupplementaryMaterialsEPSPD2000152R2.pdf](#)
- [GraphicalabstractEPSPD2000152R2.jpg](#)